

High-contrast and resolution near-infrared photometry of the core of R136

Zeinab Khorrami, Maud Langlois, Paul C. Clark, Farrokh Vakili, Anne S. M. Buckner, Marta Gonzalez, Paul Crowther, Richard Wünsch, Jan Palouš, Stuart Lumsden, et al.

▶ **To cite this version:**

Zeinab Khorrami, Maud Langlois, Paul C. Clark, Farrokh Vakili, Anne S. M. Buckner, et al.. High-contrast and resolution near-infrared photometry of the core of R136. Monthly Notices of the Royal Astronomical Society, 2021, 503, pp.292-311. 10.1093/mnras/stab388 . insu-03689267

HAL Id: insu-03689267

https://insu.hal.science/insu-03689267

Submitted on 7 Jun 2022

HAL is a multi-disciplinary open access archive for the deposit and dissemination of scientific research documents, whether they are published or not. The documents may come from teaching and research institutions in France or abroad, or from public or private research centers.

L'archive ouverte pluridisciplinaire **HAL**, est destinée au dépôt et à la diffusion de documents scientifiques de niveau recherche, publiés ou non, émanant des établissements d'enseignement et de recherche français ou étrangers, des laboratoires publics ou privés.

Monthly Notices of the ROYAL ASTRONOMICAL SOCIETY

MNRAS **503,** 292–311 (2021) doi:10.1093/mnras/stab388
Advance Access publication 2021 February 11

High-contrast and resolution near-infrared photometry of the core of R136

Zeinab Khorrami [1]★ Maud Langlois,[2] Paul C. Clark [1] Farrokh Vakili,[3,4] Anne S. M. Buckner,[5] Marta Gonzalez,[6] Paul Crowther,[7] Richard Wünsch,[8] Jan Palouš,[8] Stuart Lumsden[9] and Estelle Moraux[6]

[1]*School of Physics and Astronomy, Cardiff University, The Parade, Cardiff CF24 3AA, UK*
[2]*Universite de Lyon, Universite Lyon 1, CNRS, CRAL UMR5574, F-69561, Saint-Genis Laval, France*
[3]*Universite Cote d'Azur, OCA, CNRS, F-06304, Lagrange, France*
[4]*Department of Physics, Shahid Beheshti University, G.C., Tehran, Iran*
[5]*School of Physics and Astronomy, University of Exeter, Stocker Road, Exeter EX4 4QL, UK*
[6]*Universite Grenoble Alpes, CNRS, IPAG, F-38000 Grenoble, France*
[7]*Department of Physics and Astronomy, Hounsfield Road, University of Sheffield, Sheffield S3 7RH, UK*
[8]*Astronomical Institute of the Czech Academy of Sciences, BočníII 1401/1a, CZ-141 00 Praha 4, Czech Republic*
[9]*School of Physics and Astronomy, University of Leeds, Leeds LS2 9JT, UK*

Accepted 2021 February 5. Received 2021 February 5; in original form 2020 November 17

ABSTRACT

We present the sharpest and deepest near-infrared photometric analysis of the core of R136, a newly formed massive star cluster at the centre of the 30 Doradus star-forming region in the Large Magellanic Cloud. We used the extreme adaptive optics of the SPHERE focal instrument implemented on the ESO Very Large Telescope and operated in its IRDIS imaging mode for the second time with longer exposure time in the H and K filters. Our aim was to (i) increase the number of resolved sources in the core of R136, and (ii) to compare with the first epoch to classify the properties of the detected common sources between the two epochs. Within the field of view (FOV) of $10.8'' \times 12.1''$ (2.7 pc × 3.0 pc), we detected 1499 sources in both H and K filters, for which 76 per cent of these sources have visual companions closer than $0.2''$. The larger number of detected sources enabled us to better sample the mass function (MF). The MF slopes are estimated at ages of 1, 1.5, and 2 Myr, at different radii, and for different mass ranges. The MF slopes for the mass range of 10–300 $M_\odot$ are about 0.3 dex steeper than the mass range of 3–300 $M_\odot$, for the whole FOV and different radii. Comparing the JHK colours of 790 sources common in between the two epochs, 67 per cent of detected sources in the outer region ($r > 3''$) are not consistent with evolutionary models at 1–2 Myr and with extinctions similar to the average cluster value, suggesting an origin from ongoing star formation within 30 Doradus, unrelated to R136.

Key words: instrumentation: adaptive optics – stars: luminosity function, mass function – stars: massive – open clusters and associations: individual: R136.

1 INTRODUCTION

R136 is a very massive young star cluster that lies at the centre of the Tarantula nebula in the Large Magellanic Cloud (LMC). Hosting the most massive stars known in the Local Universe (Crowther et al. 2010, 2016), R136 provides a unique opportunity to observationally study the formation of massive stars and clusters in the earliest stages of their evolution. Our understanding of the true nature of R136 has significantly improved with increasing telescope resolution. The combination of photometry (Hunter, Shaya & Holtzman 1995; Brandl et al. 1996; Andersen et al. 2009; De Marchi et al. 2011; Cignoni et al. 2015), ultraviolet spectrometry [STIS/MAMA, Crowther et al. (2016)], and visible [*HST*/FOS, Massey & Hunter (1998)] and near-infrared (NIR) observations (VLT/SINFONI, Schnurr et al. 2009) has resulted in more constraints on the R136 stellar population and its most luminous stars.

In 2015, R136 was observed for the first time in the NIR by the second-generation Spectro-Polarimetric High-contrast Exoplanet Research[1] (SPHERE, Beuzit et al. 2019) instrument of the Very Large Telescope (VLT). Thanks to SPHERE's high-contrast and extreme adaptive optics (XAO), the sharpest images from the central region of R136 were recorded in J and K. For the first time, more than 1000 sources were detected in these bandpasses within the small field of view (FOV) of IRDIS ($10.9'' \times 12.3''$) covering almost 2.7 × 3.1 pc of R136 core (Khorrami et al. 2017). The SPHERE data on R136 core were used to partially resolve and study the initial mass function (IMF) covering a mass range of 3–300 $M_\odot$ at ages of 1 and 1.5 Myr. The density in the core of R136 ($r < 1.4$ pc) was estimated and extrapolated in 3D for larger radii (up to 6pc). Even at high angular resolution in the NIR, the stars in the core are still unresolved due to crowding and central concentration of bright sources. Using evolutionary models of stars more massive than 40 solar masses, Bestenlehner et al. (2020) find that the IMF of massive

★ E-mail: KhorramiZ@cardiff.ac.uk

[1]https://www.eso.org/sci/facilities/paranal/instruments/sphere.html

© 2021 The Author(s).
Published by Oxford University Press on behalf of Royal Astronomical Society. This is an Open Access article distributed under the terms of the Creative Commons Attribution License (http://creativecommons.org/licenses/by/4.0/), which permits unrestricted reuse, distribution, and reproduction in any medium, provided the original work is properly cited.

Downloaded from https://academic.oup.com/mnras/article/503/1/292/6133467 by CNRS - ISTO user on 07 June 2022

Table 1. Exposure time log of VLT/SPHERE observations on R136.

Obs. date	Filter	Single/Total Exposure(s)	λ_{cen}(nm)	$\Delta\lambda$ (nm)
2015-09-22	BB-J	4.0/1200	1245	235
2015-09-22	BB-K	4.0/1200	2182	294
2018-10-10	BB-K	4.0/4352	2182	294
2018-11-14	BB-H	2.0/4352	1626	286

stars in R136 is top heavy with a power-law exponent $\gamma = 2.0 \pm 0.3$. They also estimate the age of R136 between 1 and 2 Myr with a median age of around 1.6 Myr.

This paper presents the second epoch observation of R136 in the NIR by VLT/SPHERE. These observations, obtained with longer exposures in different NIR filters, aimed first to increase the number of resolved sources in the core of R136, and second to enable comparison with the first epoch to classify the property of the detected common sources between these two epochs. We divided this paper as follows. In Section 2, we explain in detail the data and the observing conditions. We then present the photometric analysis in Section 3 and the method we use to correct for completeness in Section 4. In Section 5, we describe the details of extinction estimation. On the basis of the results, we investigate the stellar mass functions (MFs) and the density in Section 6. In Section 7, we compare the photometric analysis between the two epochs and between the two sets of filters. We conclude by summarizing our results in Section 8.

2 OBSERVATIONS

We obtained the data via ESO Time Observation run (0102.D-0271) to image R136 using the 'classical imaging' mode of IRDIS Langlois et al. (2014) in H- and K-bandpass filters. For our purpose, we used the same spectral band split into the two IRDIS channels to correct for residual detector artefacts such as hot pixels and uncorrelated detector noise among other instrumental effects. We maximized the image sharpness of the total exposure by discarding the single frames with poorer Strehl ratio (SR) and by correcting 'a posteriori' the residual tip-tilt image motion on each short exposure before combining them. Observations were performed in October/November (K/H) 2018, achieving high dynamical range and high angular resolution imaging in both the H and K bandpass, over a FOV of $10.8'' \times 12.1''$ (2.7 pc $\times$ 3.0 pc), centred on the core of the cluster. The natural seeing was 0.69 ± 0.10 arcsec in K and 0.58 ± 0.05 arcsec in H during the observations. The night was rated as 'Clear' meaning that less than 10 per cent of the sky (above 30° elevation) was covered by clouds, and the transparency variations were less than 10 per cent during the exposures.

Our data consist of 1088/544 frames of 2.0/4.0 s exposures taken with the IRDIS broad-band H and K filters (BB-H, BB-K). Table 1 shows the exposure time log of the two epoch observations and the filters information. Fig. 1 shows the final reduced images in the H (left) and the K (right). These images are the deepest and sharpest images taken from the core of R136 so far. The Wolf–Rayet (WR) star R136a1 was used for guiding the AO loop of SPHERE confirming the high level of performances even for faint guide stars that surpass both NACO and MAD performances. Fig. 2 compares the highest resolution available images from the very central part of R136 taken by *HST* (WFPC2 by Hunter et al. 1995) in left (top in V, bottom in H), VLT/MAD (Campbell et al. 2010) in the middle (top in K, bottom in H), and IRDIS in right (top in K, bottom in H). These images show the effect of better contrast, pixel-sampling, sensitivity, and AO correction on resolving the stellar sources in the most crowded part of R136.

The range of airmass during these observations was 1.52 –1.45 in K, and 1.70–1.55 in the H. A log of observations is provided in Table 2. For comparison, we include the observing log for our first epoch data sets taken in 2015.

We used the SPHERE pipeline package to correct for dark (current), flat (fielding), (spatial) distortion, bad pixels, and thermal background due to instrument and sky (in K). Furthermore, and in order to reach the highest sensitivity and the largest number of detectable sources, additional corrections were carried out on the images. Based on a Gaussian fit using selected stars, we estimated and corrected the subpixel image drifts before combining the individual images. This allowed us to correct for residual tip-tilt errors with an accuracy of a few mas. The final step is performed to combine the parallel images on the left and right sides of the detector, after the anamorphism correction. Some uncorrected background leaks persist in our final K images due to thermal background fluctuations, which are stronger in K than in H.

3 PHOTOMETRY

To analyse the final images, we applied the same method/tools as on first epoch data (Khorrami et al. 2017). For the photometry, we used the *Starfinder* package implemented in Interactive Data Language (IDL, Diolaiti et al. 2000). *Starfinder* is designed for the analysis of AO images of crowded fields, like the Galactic Centre, for instance, as in Pugliese et al. (2002). This method determines the empirical local point spread function (PSF) from several isolated sources in the image and uses this PSF to extract other stellar sources across the FOV.

For the present study, four and seven well isolated stars (within $0.47'' \times 0.47''$) were used to extract the PSF in the K and H, respectively. The FOV in K is more crowded than in H (see Fig. 1), so finding the bright isolated stars (within $0.47'' \times 0.47''$) in K is harder than in H. That is why we limit our selection of stars to be used for PSF extraction to four in K. Fig. A3 shows the separation with the closest neighbour for each star in H and K. The extracted PSFs were used as an input for stellar sources detection by *Starfinder*. The full width at half-maximum (FWHM) of the extracted PSFs are 58.8 and 63.7 mas in H and K, with 1658 and 2528 sources detected, respectively. We stopped the source extraction after obtaining a minimum correlation coefficient of 65 per cent and 80 per cent, in K and H, between the extracted star with the locally determined PSF according to *Starfinder* procedures. In H, we put a higher threshold on minimum correlation coefficient than in K, because the AO correcting efficiency in H degrades faster as a function of distance from R136a1 – which is the reference star for the AO loop – than in K. The isoplanatic angle in H is smaller than in K, so at larger radii from R136a1, the PSF is not centrosymmetric. Indeed, stars with higher correlation coefficients, i.e. more similarity to the PSF, represent higher reliability on their photometry estimation.

In addition to the correlation coefficient criterion, we applied the limit of standard deviation from the sky brightness (σ_{sky}) for stopping the extraction of sources by *Starfinder*, i.e. the local PSF maximum value must exceed $2\sigma_{sky}$ over the background. Fig. 3 shows the signal-to-noise ratio (SNR) of 1658 and 2528 detected sources in H (purple circles) and K (green squares), respectively. Common sources (1499) between H and K are shown as filled circles/squares. The solid horizontal line shows the SNR = 2.0 where some of the detected sources have SNR less than this value. These stars are located further from the central region where the local σ_{sky} is smaller than the σ_{sky} of

Downloaded from https://academic.oup.com/mnras/article/503/1/292/6133467 by CNRS - ISTO user on 07 June 2022

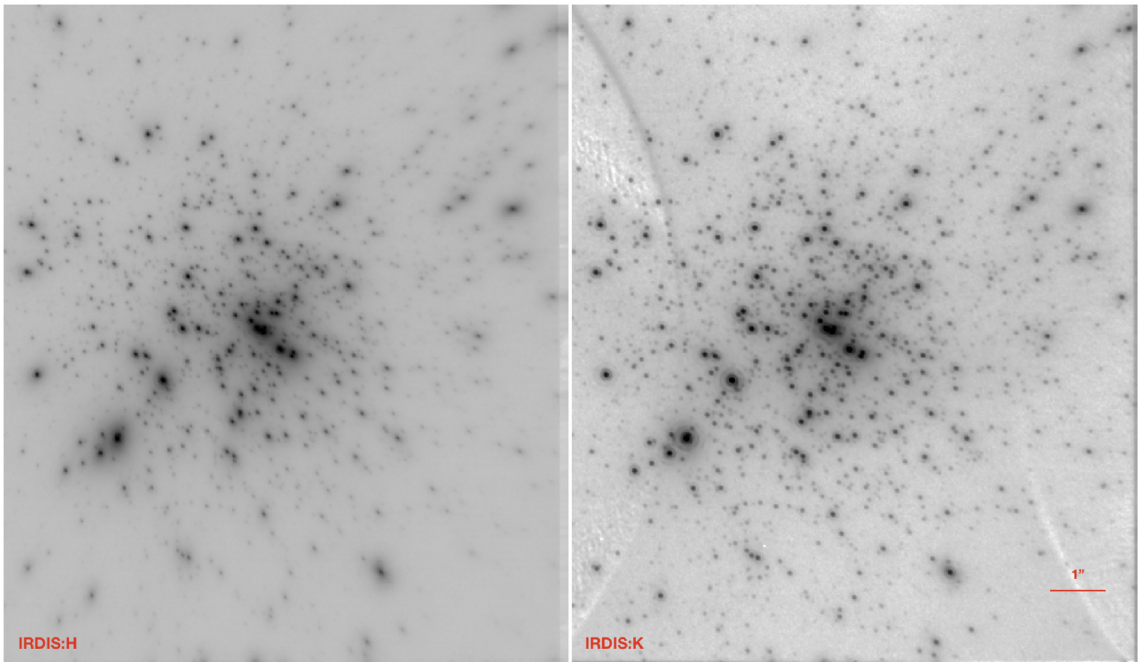


Figure 1. R136 core images taken by VLT/SPHERE/IRDIS in the H (left) and the K (right). FOV is $10.8'' \times 12.1''$.

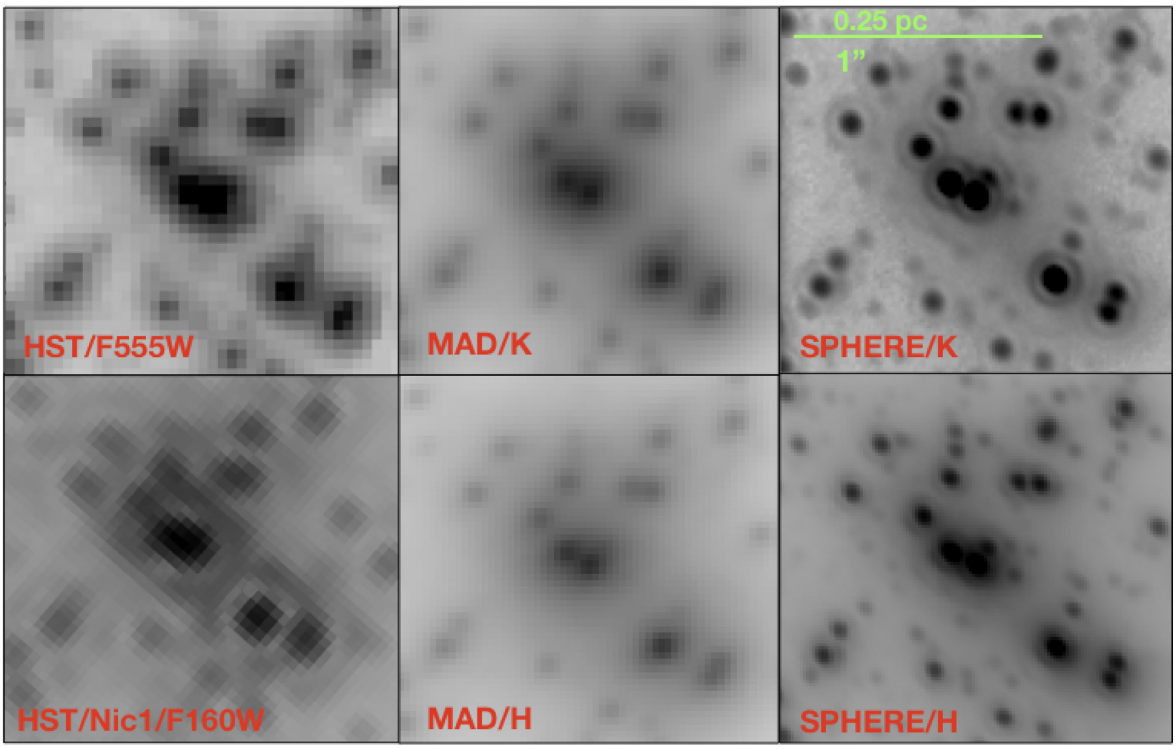


Figure 2. Comparison of R136 central images at different wavelengths with the highest available angular resolution telescopes. Top, left to right: *HST*/WFPC2 in V , VLT/MAD in K, and VLT/SPHERE in K. Bottom, left to right: *HST*/NICMOS/NIC1, VLT/MAD, and VLT/SPHERE in the H. The identification of bright sources is shown in Fig. A2.

the whole FOV. 76 per cent of these sources have visual companions closer than $0.2''$, which is much higher than the value found in the first epoch in 2015 data. Fig. 4 shows the histogram of closest neighbour (visual companion) separation from each source versus its distance from the centre of R136, in 2015 (top) and 2018 (bottom) data. Comparing the histogram of closest companions between two epochs, 85 per cent of the new detected sources in 2018 have visual companions with separation less than $0.2''$.

The SR in H and K is determined as 0.71 ± 0.05 and 0.83 ± 0.03, respectively, on average within 5 arcsec from the core. These

Downloaded from https://academic.oup.com/mnras/article/503/1/292/6133467 by CNRS - ISTO user on 07 June 2022

Table 2. Observing condition for R136 data in 2015 and 2018.

Data	SR	Seeing(")	Airmass	N_{phot}
2015-J	0.40 ± 0.05	0.63 ± 0.1	1.54–1.59	1110
2015-K	0.75 ± 0.03	0.63 ± 0.1	1.61–1.67	1059
2018-H	0.71 ± 0.05	0.58 ± 0.05	1.70–1.55	1658
2018-K	0.83 ± 0.03	0.69 ± 0.10	1.52–1.45	2528

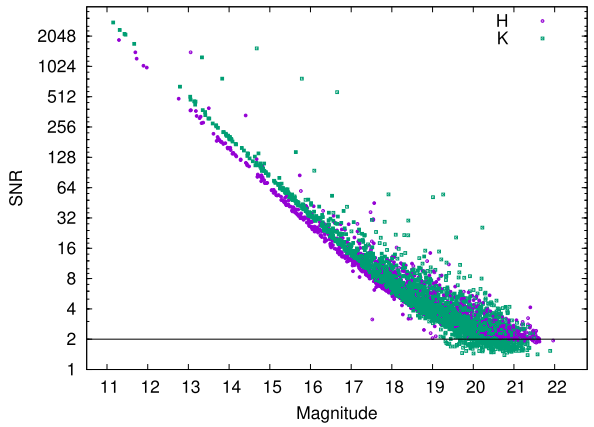


Figure 3. Signal-to-noise ratio of detected sources in H (purple circles) and K (green squares) versus their magnitudes. Filled dots are common sources between H and K data. The solid horizontal line shows the SNR = 2.0.

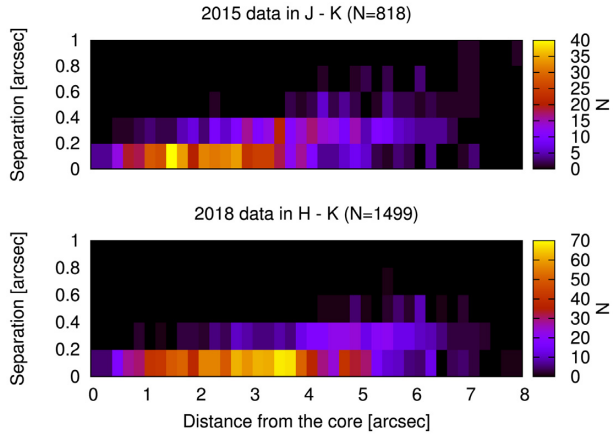


Figure 4. Histogram of the separation of the close detected sources versus their distance from the core of R136. Top: 818 common sources between J and K data in 2015. Bottom: 1499 common sources between H and K data in 2018.

estimates are assessed from the SPARTA files recorded during SPHERE runs simultaneously with the AO-corrected images of R136. They are based on the slope measurements of the Shack–Hartmann wavefront sensor in Sphere AO for eXoplanet Observation (SAXO) by extrapolating the phase variance deduced from the reconstruction of SAXO open-loop data using deformable mirror, tip-tilt voltages, and wavefront sensor closed-loop measures (Fusco et al. 2004). The method has been proved quite robust for FOV smaller than the anisoplanetism in the past for differential imaging by NACO (Maire et al. 2014). We are therefore quite confident on our photometry corrected for the SR effect in H and K. To convert stellar fluxes to magnitudes, we set the zero-point magnitude to the instrumental zero-point (one ADU/s in H and K, are 25.2 and 24.8 magnitudes, respectively). To double check our calibration, we compared H and K magnitudes of 26 sources (located $r \geq 3''$ from R136a1) common between our catalogue and the VLT/MAD (Campbell et al. 2010) in H and K.[2] We cannot compare our zero-points with the MAD/H and K magnitudes in the central 2.8″ region because of the completeness issue and the very low AO correction (SR ∼ 15–30 per cent) of their data. Fig. 2 shows the completeness and contrast problem of the previous data, leading to an inability to distinguish certain sources. By way of example R136a6 (H19) and H26[3] – are very close in terms of brightness (flux ratio of about 90 per cent) and location (separation of about 70 mas). These bright O-type stars are most easily detectable in our data compared with others (Figs 2 and A2). Cases like these close bright stars, bring confusion even in the *HST* spectroscopic analysis (Bestenlehner et al. 2020).

The K magnitude of R136a1 and R136a2 (11.15 mag and 11.43 mag) increased about 0.08 and 0.11 mag, compared to their K mag in the first epoch (11.07 mag and 11.32 mag). The brightness of R136a3 and R136b in K (11.45 mag and 11.67 mag) is consistent with the first epoch K data (11.44 mag and 11.66 mag). R136c in the K (11.31 mag) is 0.17 mag brighter than in 2015 (11.48 mag), making this source the second brightest in our K catalogue. In previous studies, R136c shows indications of binarity based on its strong X-ray emission (Portegies Zwart, Pooley & Lewin 2002; Townsley et al. 2006; Guerrero & Chu 2008) and possible low-amplitude RV variations (Schnurr et al. 2009).

Comparing the brightness of common detected sources within two epochs, the K magnitude of 56 per cent of the sources has changed more than twice their photometric errors.[4] To make sure that this is not due to *Starfinder* photometry analysis (which is based on the reference input PSF), we have used DAOPHOT algorithm for this analysis as well. The variation of the K magnitude of these sources still remains.[5] The K mag of about 67 per cent of the sources located outside of the core ($r > 3''$) has changed more than twice their photometric errors. Since the observations were made in different nights and the AO correction in the outer part of the FOV is not as good as its centre, this inconsistency is probably an observational effect; otherwise, it is originated from physical reasons like variables or multiple systems with periods less than 3 yr.

4 COMPLETENESS

We produced 6.2×10^4 artificial stars (500 per magnitude) in H and K, in order to determine the completeness as a function of magnitude. These artificial stars are created using the same PSF as we used for source extraction process. They are added to the original image one by one (500 times per magnitude) and the same photometric tools and criteria to determine how often they can be recovered from the source extraction process are used. These tests were performed one star at a time to avoid the artificial stars from affecting one another. Fig. 5 shows the completeness values as a function of magnitude in H (purple dots) and K (green squares). The completeness is 80 per cent at $K = 20$ mag and $H = 20.5$ mag.

[2]See the comparison between two catalogues in Fig. A7.
[3]Identification from Hunter et al. (1995) – see Fig. A2 to check the position of these stars in the core.
[4]See Fig. A4 to compare the K mag of these sources within two epochs.
[5]See Fig. A5 to compare the photometric analysis using *Starfinder* and DAOPHOT.

Downloaded from https://academic.oup.com/mnras/article/503/1/292/6133467 by CNRS - ISTO user on 07 June 2022

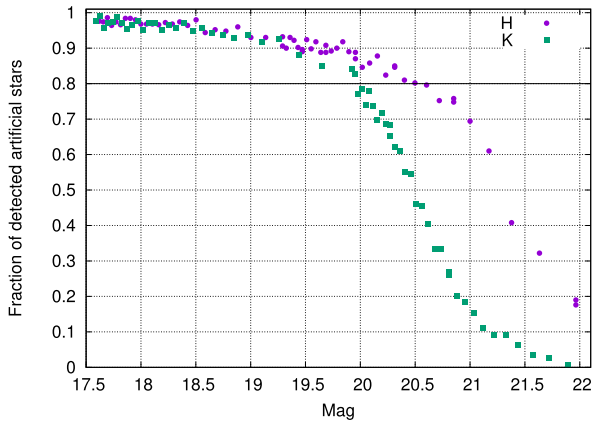


Figure 5. Average value of completeness values for the whole FOV as a function of magnitude using 62 000 artificial stars in H (purple dots) and K (green squares).

The completeness value in each magnitude is the average value for detection of 500 artificial stars that are distributed randomly in the FOV. But the completeness varies across the FOV depending on how crowded and bright that region is. Using these 6.2×10^4 artificial stars, we created completeness maps covering magnitude range of 17–22 (five maps), both in H and in K. Fig. 6 shows two examples of completeness map in the magnitude of 19–20 both in H (top) and in K (bottom). The average value of completeness is about 90 per cent both in H and in K (Fig. 5), but one can notice that the completeness in the very central part of the cluster is much lower than the outskirts. In the K, we can also see the effect on the completeness of the thermal background noise from the instrument lying in the arcs located in the far east and west parts of the FOV as seen in Fig. 6. The black pluses in Fig. 6 shows the position of the observed sources (398 in H and 410 in K) within the magnitude range of 19–20. This plot clearly shows the effect of completeness on the detected sources that are used to create MF. To overcome this limitation, we corrected the MF for all stars fainter than 17 magnitude. Each star contributes a mass distribution to the MF (see Section 6). When we added stars with a given mass to the histogram of mass, we corrected the contribution of each star to the MF (fainter than 17 mag) for completeness using the completeness maps in every H and K magnitudes. We know that the completeness in a given magnitude varies across the FOV in both filters, so depending on the position and magnitude of an observed star, we estimated its completeness using these maps (see Fig. 6). Since the average value of completeness at 17 mag is above 95 per cent (above 80 per cent at the core), we stopped the completeness correction for sources brighter than $K = 17$ mag.

5 EXTINCTION

In order to fit the evolutionary models to our data and estimate the stellar masses, we need to measure the extinction first. We used two methods to estimate the extinction for the spectroscopically observed massive stars in the core of R136.[6] In both methods, we adopt the LMC distance modulus (DM) of 18.49 magnitude estimated by

[6]List of spectroscopically known stars is provided in Table A1. List of stars brighter than 16 mag in K (138 sources) is provided in Table A2 with their SPHERE (J, H, and K) and *HST* (U, V, and B) magnitudes. See Fig. A2 to check the position of these sources in our data.

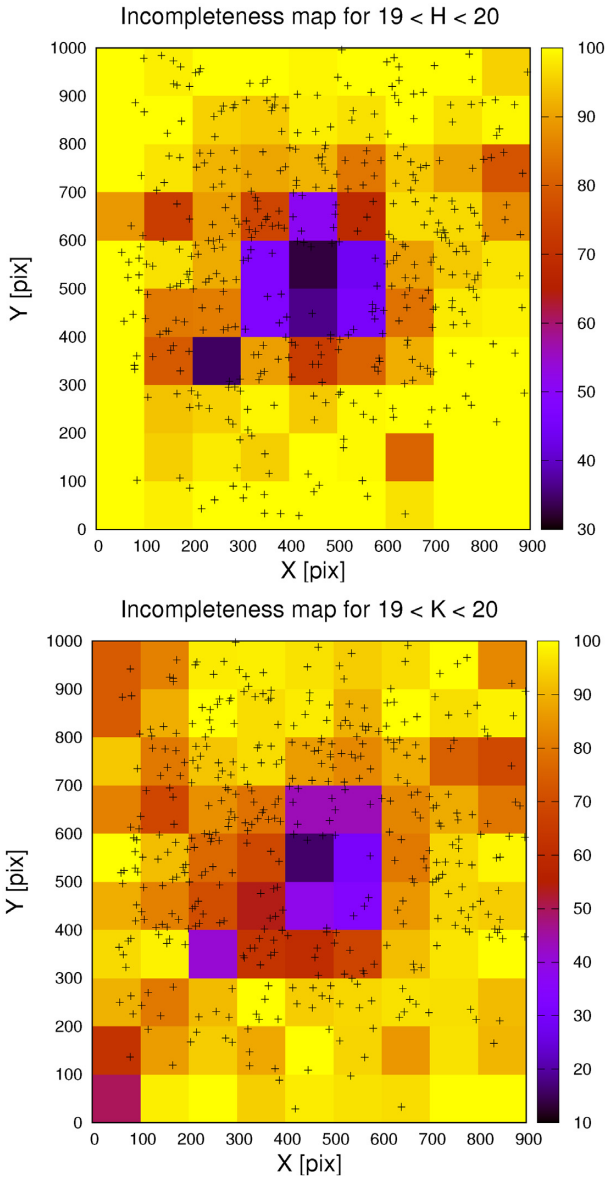


Figure 6. Completeness map for magnitude range of 19–20 in H (top) and in K (bottom). Black pluses shows the position of photometric detected sources within the given magnitude range. colour shows completeness in percents.

Pietrzyński et al. (2013), which is consistent with the value suggested by Gibson (2000) for LMC.

Method I: We used the effective temperature ($T_{\rm eff}$) and luminosity (logL) of 49 stars by Bestenlehner et al. (2020) in the optical. The values of these temperatures and luminosities are provided in Table A1. We also chose a grid of isochrones at different ages (from 0.1 up to 10 Myr) with the LMC metallicity ($Z = 0.006$) from the latest sets of PARSEC evolutionary model[7] Bressan et al. (2012), which is a complete theoretical library that includes the latest set of stellar phases from pre-main sequence to main sequence and covering stellar masses from 0.1 to 350 $M_\odot$. By fitting the PARSEC isochrones to the observed stellar parameters of each star ($T_{\rm eff}$, logL), we estimated the age and intrinsic colour for each star with an error.

[7]http://stev.oapd.inaf.it/cgi-bin/cmd, YBC version of bolometric corrections as in Chen et al. (2019).

Downloaded from https://academic.oup.com/mnras/article/503/1/292/6133467 by CNRS - ISTO user on 07 June 2022

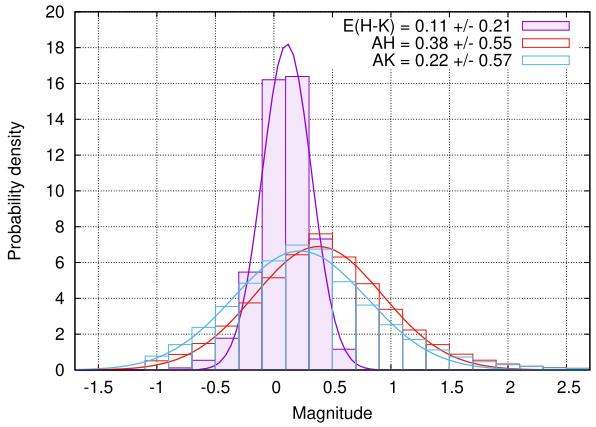


Figure 7. Histogram of extinction in H and K filters from observations using 49 spectroscopically known stars (Bestenlehner et al. 2020) in the FOV.

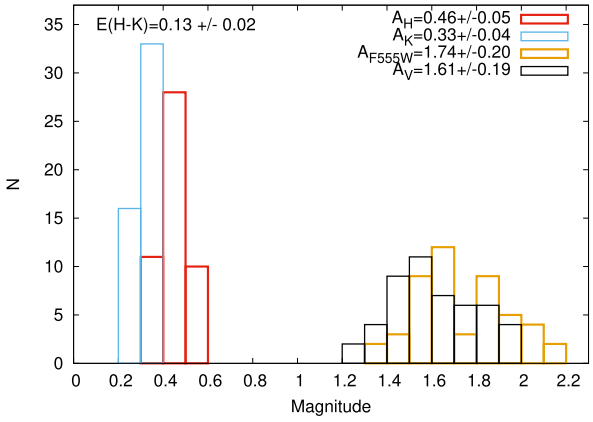


Figure 8. Histogram of extinction in H and K filters modelled based on observed stellar parameters of $T_{\rm eff}$, logL, and logg from Bestenlehner et al. (2020) and A_{F555W} from Crowther et al. (2016).

The extinction in H and K ($A_{\rm H}$ and $A_{\rm K}$) is estimated by comparing these intrinsic H and K magnitudes with the observed values from our catalogue. Fig. 7 shows the histogram of the extinction values of those 49 stars. The mean extinction in H and K and the mean colour excess are $A_{\rm H} = 0.38 \pm 0.55, A_{\rm K} = 0.22 \pm 0.57$, and $E(H-K) = 0.11 \pm 0.21$. These values derived by fitting a Gaussian function on the extinction distributions, while these distributions are not exactly Gaussian and symmetric. That is why the mean colour excess is slightly (0.05 mag) higher than $A_{\rm H} - A_{\rm K}$. The large errors on these values result from the errors in the reported stellar parameters ($T_{\rm eff}$ and log L) from the spectroscopic analysis in the optical (see Table A1).

Method II: Using the stellar parameters from Bestenlehner et al. (2020), we adopt the closest stellar atmosphere model of that star. We used the grids of TLUSTY[8] atmosphere models (Hubeny & Lanz 1995) for O-type (Lanz & Hubeny 2003) stars with the LMC metallicity ($Z = 1/2Z_{\odot}$). The apparent magnitudes of these stars in the SPHERE/IRDIS H and K filters are calculated by MYOSOTIS[9] (Khorrami et al. 2019). We adopt A_{F555W} for these sources from Crowther et al. (2016) as an input for MYOSOTIS to estimate the H and K magnitudes of these stars using the synthetic extinction curves[10] from Draine (2003a, 2003b, 2003c), Li & Draine (2001), and Weingartner & Draine (2001) for $R_V = 4.0$. The simulated H and K magnitudes of 55 per cent (85 per cent) of these sources (except for three WRs) are less than 0.1 (0.2) magnitudes different from the observed values. The simulated extinction and colour excess of these 49 stars in H and K are $A_{\rm H} = 0.46 \pm 0.05, A_{\rm K} = 0.33 \pm 0.05$, and $E(H - K) = 0.13 \pm 0.02$, shown in Fig. 8. One can compare the result of these simulations with observation in Fig. 9 (top), where black circles are 49 spectroscopically known stars from Bestenlehner et al. (2020) and black squares are their simulated magnitudes.

The colour excess, $E(H - K)$, estimated by two methods is consistent, and the extinction values, $A_{\rm H}$ and $A_{\rm K}$, in *Method II* are 0.1 mag higher than in *Method I*. We adopt the extinctions of $A_{\rm H} = 0.45$ and $A_{\rm K} = 0.35$ magnitudes, which are consistent with the two analyses (within the error bars) and De Marchi & Panagia (2014). The colour excess of $E(H - K) = 0.1$ is also consistent with Tatton et al. (2013) and with the one used in previous studies by Campbell et al. (2010).

[8]http://nova.astro.umd.edu/Tlusty2002/tlusty-frames-cloudy.html
[9]Star cluster simulator tool https://github.com/zkhorrami/MYOSOTIS
[10]www.astro.princeton.edu/~draine/dust/dustmix.html

6 MASS FUNCTION AND CORE DENSITY

Fig. 9 shows the colour magnitude diagram (CMD) of 1499 detected sources common between the H and K data (top) for the full FOV in left ($N = 1499$), for inner $r < 3''$ region ($N = 627$) in middle, and for outer $r > 3''$ region ($N = 872$) in right.[11] Red, yellow, and blue solid lines are PARSEC isochrones at DM = 18.49 with $A_{\rm K} = 0.35$ and $E(H - K) = 0.1$ at the ages of 1, 1.5, and 2 Myr, respectively. We note that there is a large scatter in the CMD, especially for the lower part of the main-sequence and pre-main-sequence sources, which are located (detected) in the outer region. A significant scatter in CMD and colour–colour diagrams of 30 Doradus has previously been reported in the visible and NIR (Hunter et al. 1995; Andersen et al. 2009; De Marchi et al. 2011; Cignoni et al. 2015). The scatter is likely due to a combination of observational confusion (affected mainly by the visual multiple systems or variables), photometric errors, differential extinction, a possible age spread, colour excess due to warm circumstellar matter, and ongoing star formation within 30 Doradus. Pre-main-sequence stars are often associated with circumstellar discs and outflows, which will introduce additional extinction for the clusters low-mass content. Brandl et al. (1996) found that the extinction varies significantly from star to star within the cluster, with the range of 1–2 mag. The *HST* observations also reveal the presence of considerable differential extinction across the 30 Doradus region. De Marchi et al. (2011) quantified the total extinction towards massive main-sequence stars younger than 3 Myr to be in the range of $1.3 < A_{\rm V} < 2.1$. Fig. 9 shows that the evolutionary models (isochrones) cannot be fitted for these scattered sources. We prefer to consider an (larger) error of 0.5 mag on the extinction to estimate the stellar mass range for each star at a given age. We estimated the stellar masses just for common sources between H and K data (1499 sources) using both their H and K magnitudes fitted to PARSEC isochrones at three different ages: 1, 1.5, and 2 Myr.

The MF is plotted in Fig. 10 considering a Gaussian distribution for each stellar mass. We convert the photometric/extinction uncertainty into a mass (Gaussian) distribution. This Gaussian uncertainty in the mass of each star is accounted for, when constructing the MF.

[11]In the first epoch data, in J data, the PSF is not centrosymmetric at large distances from R136a1, starting typically around $3''$ (approximately half of FOV radius). For the sake of comparison of two epochs, we choose $r = 3''$ for analysing detected sources in/out of this radius.

Downloaded from https://academic.oup.com/mnras/article/503/1/292/6133467 by CNRS - ISTO user on 07 June 2022

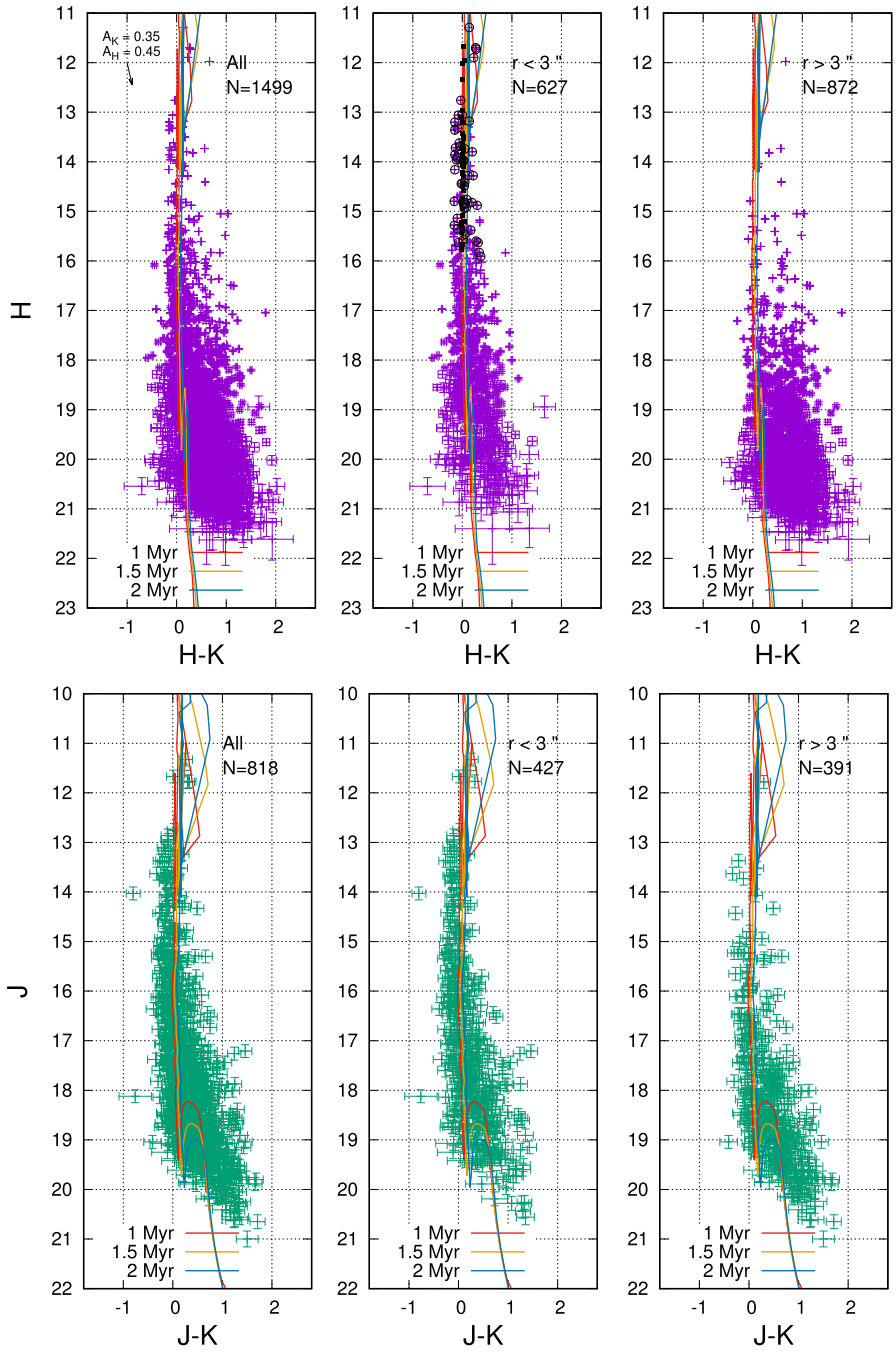


Figure 9. Top: CMD of detected sources common between the H and K data for the full FOV in left ($N = 1499$), for central $r < 3''$ region ($N = 627$) in middle, and for outer $r > 3''$ region ($N = 872$) in right. Red, yellow, and blue solid lines are PARSEC isochrones at DM = 18.49 with $A_K = 0.35$ and $E(H - K) = 0.1$ at the ages of 1, 1.5, and 2 Myr, respectively. The black circles are the 49 spectroscopically known stars from Bestenlehner et al. (2020) and the black squares represent the simulated magnitudes for these 49 sources (explained in Section 6: *Method II*). Bottom plots are same as top plots but for 818 sources detected in J and K in our first epoch observation (Khorrami et al. 2017).

Each star fainter than $K = 17$ (about 13.4 $M_\odot$ at 2 Myr) is corrected for completeness, according to its brightness and its location in the FOV (see Section 4 for more information). Fig. 10 shows the MF at three different ages (1, 1.5, and 2 Myr) for the whole FOV (top), central $r \leq 3''$ region (middle), and outer $r > 3''$ region (bottom). The MF slope values in these regions, at different ages and mass ranges, are provided in Table 3, both for the completeness-corrected (Γ_{CC}) and not corrected MF (Γ_{NC}). The MF slopes are calculated for the minimum mass of 3 $M_\odot$ (about $K = 19.8$ at 2 Myr) where the average value of completeness is above 85 per cent (Fig. 5) but the difference between Γ_{CC} and Γ_{NC} is not negligible for the inner region of the cluster where the completeness reaches to 30 per cent (see Fig. 6) and this affects the MF slope for the whole FOV (top values in Table 3). The slopes for the mass range of 3–300 $M_\odot$ for the inner region are flatter than those for the outer region and consequently for the whole FOV. This can be explained by completeness since

Downloaded from https://academic.oup.com/mnras/article/503/1/292/6133467 by CNRS - ISTO user on 07 June 2022

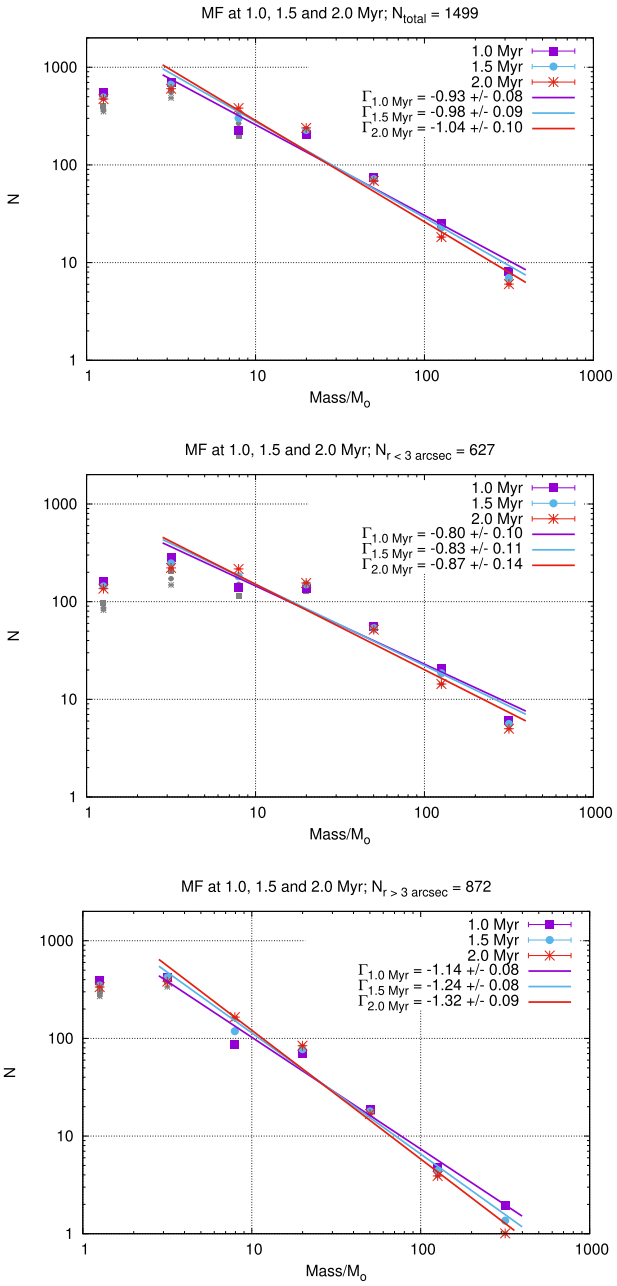


Figure 10. Mass function at 1, 1.5, and 2 Myr for the whole FOV (top), central $r < 3''$ region (middle), and outer region $r > 3''$ (bottom). Grey symbols are the values without completeness correction. See Table 3 for the MF slopes values.

the Γ_{CC} and the Γ_{NC} are not compatible. But for the mass range of 10–300 $M_\odot$ where the data are complete (see Figs 5 and A1) and the MFs are not affected by completeness (compare Γ_{CC} and Γ_{NC} in Table 3), the slope values in the inner region are slightly flatter than those in the outer region and consequently than the whole FOV. Comparing the stellar population in the inner region with the outer region in CMD (Fig. 9), detected sources are compatible with the evolutionary models in the inner region [Fig. 9 (top middle)], but for the outer region, detected sources differ from the isochrones. About 50 per cent of the high-mass stars are located in the right side of the main sequence, far from the evolutionary models. If these population truly belong to R136, then they have K bandpass excess emission due

Table 3. Γ_{CC} is the slope of the completeness-corrected MF and Γ_{NC} is the not-corrected one. The stellar masses are estimated using parsec isochrones with DM = 18.49, $A_K = 0.35$, and $E(H-K) = 0.1$ at different ages (first column) and mass ranges (second column) for the whole FOV (top), and central $r < 3''$ region (middle), and outer $r > 3''$ region (bottom). N is the number of detected sources and N_C is the number of stars fainter than $K = 17$ mag that are corrected for completeness according to their position on the image and their brightness (see Section 4).

Age (Myr)	Mass range ($M_\odot$)	Γ_{CC}	Γ_{NC}
	All, $N = 1499$, $N_C = 1226$		
1.0	3–300	-0.93 ± 0.08	-0.89 ± 0.09
1.5	3–300	-0.98 ± 0.09	-0.94 ± 0.10
2.0	3–300	-1.04 ± 0.10	-0.99 ± 0.11
1.0	10–300	-1.17 ± 0.02	-1.16 ± 0.03
1.5	10–300	-1.26 ± 0.01	-1.25 ± 0.01
2.0	10–300	-1.34 ± 0.03	-1.33 ± 0.03
	$r < 3''$, $N = 627$, $N_C = 444$		
1.0	3–300	-0.80 ± 0.10	-0.74 ± 0.12
1.5	3–300	-0.83 ± 0.11	-0.76 ± 0.14
2.0	3–300	-0.87 ± 0.14	-0.79 ± 0.16
1.0	10–300	-1.12 ± 0.06	-1.10 ± 0.06
1.5	10–300	-1.19 ± 0.03	-1.17 ± 0.03
2.0	10–300	-1.26 ± 0.03	-1.24 ± 0.03
	$r > 3''$, $N = 872$, $N_C = 782$		
1.0	3–300	-1.14 ± 0.08	-1.13 ± 0.08
1.5	3–300	-1.24 ± 0.08	-1.22 ± 0.08
2.0	3–300	-1.32 ± 0.09	-1.30 ± 0.10
1.0	10–300	-1.31 ± 0.08	-1.31 ± 0.08
1.5	10–300	-1.47 ± 0.06	-1.47 ± 0.05
2.0	10–300	-1.60 ± 0.05	-1.59 ± 0.04

to hot dust (K-excess sources). The MF slopes in the outer region are complete for both the mass ranges and the slope values are steeper than the inner region but might be the effect of the existence of these K-excess sources.

The MF slopes for the massive part ($M > 10\ M_\odot$) in the inner region are in line with Bestenlehner et al. (2020) ($\gamma \sim 2.0 \pm 0.3$) and for the whole, FOV is consistent with Schneider et al. (2018) ($\gamma \sim 1.90^{+0.37}_{-0.26}$) for the 30 Doradus region, considering the large error bars from these studies. Massey & Hunter (1998) found the MF slope of $-1.4 < \Gamma < -1.3$ for the mass range of 15–120 $M_\odot$, which is consistent with the slope for the whole FOV at 2 Myr.

To check the presence of mass segregation, we used the minimum spanning tree (MST) algorithm by Allison et al. (2009) comparing the length of the MST connecting massive stars to that connecting randomly selected stars. Mass-segregation ratio (Λ_{MSR}, equation 1 in Allison et al. 2009) defined as the average random path length of the MST and that of the massive stars. N_{MST} is the number of selected massive stars and randomly selected stars. Fig. 11 shows Λ_{MSR} calculated for different N_{MST} subsets. Λ_{MSR} reaches to a constant value when N_{MST} is larger than the total number of massive stars ($m > 10\ M_\odot$) in the FOV, which is about 339 using 1.5-Myr isochrones. The bottom plot in Fig. 11 shows the Λ_{MSR} calculated within different radii of the cluster, centred at R136a1. The numbers within parentheses denote the total number of stars more massive than 10 $M_\odot$, which are chosen for N_{MST}. The colour shows the ratio of number of massive stars ($m > 10\,M_\odot$) to the total number of stars (down to 1 $M_\odot$) within each radius. This plot shows the variation of Λ_{MSR} locally for different sample of N_{MST}. Λ_{MSR} is less than 1.2 within the whole FOV and for $N_{MST} > 350$, and it is larger than 1.0 in all the conditions. The values of Λ are point to a moderate but significant (above 2

Downloaded from https://academic.oup.com/mnras/article/503/1/292/6133467 by CNRS - ISTO user on 07 June 2022

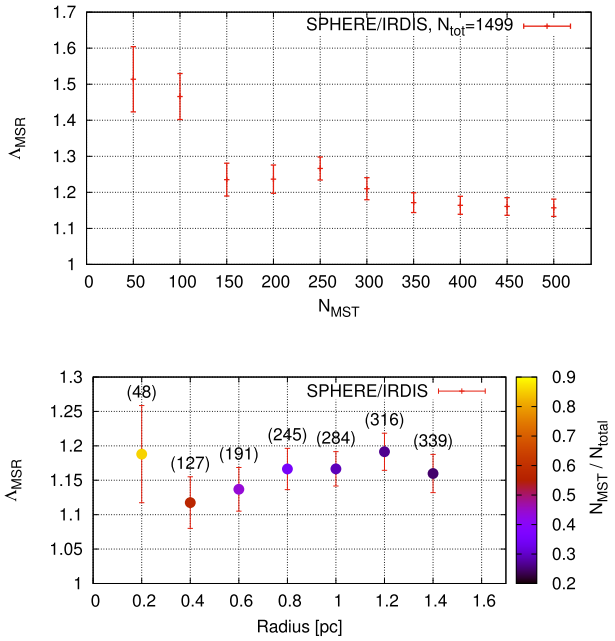


Figure 11. Top: the mass-segregation ratio ($\Lambda_{\rm MSR}$) calculated for different $N_{\rm MST}$ subsets. Bottom: $\Lambda_{\rm MSR}$ calculated within different radii of the cluster, centred at R136a1. The numbers within parentheses denote the total number of stars more massive than 10 $M_\odot$, which are chosen for $N_{\rm MST}$. The colour shows the ratio of number of massive stars ($m > 10\,M_\odot$) to the total number of stars within each radius.

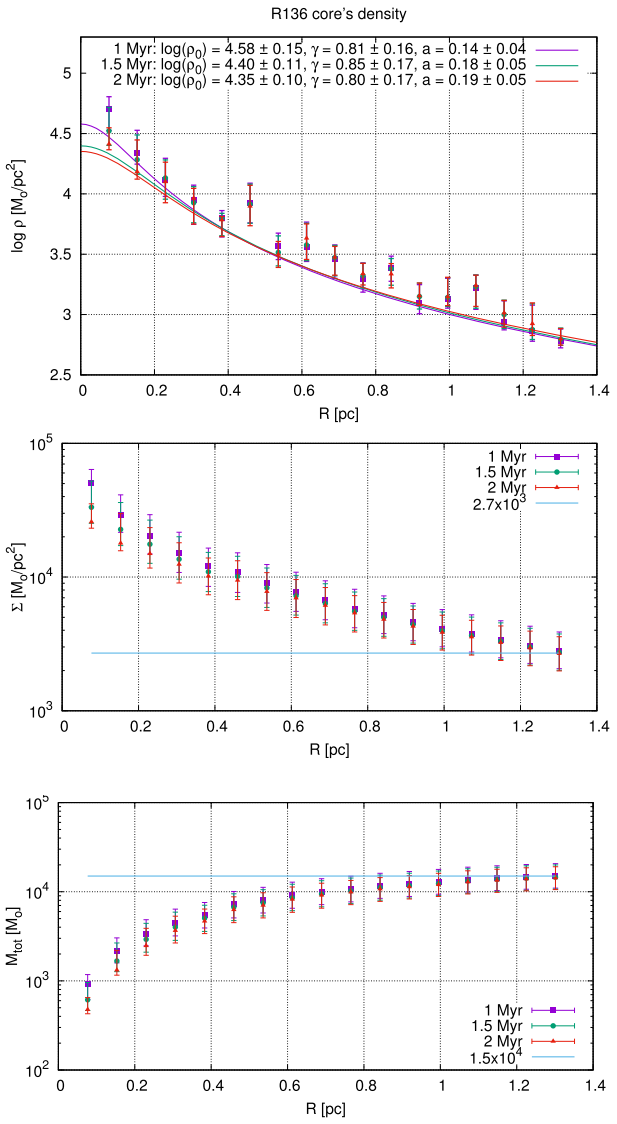


Figure 12. Top: Projected mass density (ρ) profile of R136 in IRDIS FOV centred on R136a1, using 1499 stars in H–K. The stellar masses are estimated at the age of 1 (purple squares), 1.5 (green circles), and 2 Myr (red triangles) with extinction values of $A_{\rm K} = (0.35 \pm 0.5)$ mag, $E(H-K) = (0.1 \pm 0.1)$ mag in H and K. Equation (1) is used to fit the purple, green, and red solid lines to the data at 1, 1.5, and 2 Myr, respectively. Centre: Surface densities (Σ) within a given radius. Bottom: Total stellar masses ($M_{\rm tot}$) within a given radius. Solid blue lines show the average value of surface density ($\Sigma = 2.7 \times 10^3\,M_\odot\,{\rm pc}^{-2}$) and total mass ($M_{tot} = 1.5 \times 10^4\,M_\odot$) up to $R_{max} = 1.3$ pc.

sigma) degree of mass segregation. This must be taken with caution, considering the spatial distribution of completeness (Fig. A1). The fact that, globally, we detect less low-mass stars towards the centre of the cluster can have an effect on the mass segregation ratio. If more low-mass stars are injected in the centre of the cluster, the size of the N most massive stars would still be the same, but the average size of a group of N stars within the complete sample is expected to decrease. The values of $\Lambda_{\rm MSR}$ would also decrease in that case, but quantifying this is out of the scope of this work.

Still, these MF slopes in our study are limited to the resolution of the instrument (55 mas in K) and in future, using higher angular resolution data, we may resolve binaries and low-mass stars, which affects the shape of MF.

Using the stellar masses estimated at the age of 1, 1.5, and 2 Myr, which are corrected[12] for the completeness (for 1226 sources), we plot the 2D (projected) mass density at a given radius, i.e. the mass between r and $r + dr$ divided by the corresponding area [ρ, Fig. 12 (top)]. We used an Elson–Fall–Freeman profile Elson, Fall & Freeman (1987) to fit ρ in the core of R136 (equation 1) up to the maximum radius of $R_{\rm max} = 1.32$pc from R136a1.

$$\rho[{\rm M}_\odot\,{\rm pc}^{-2}] = \frac{\rho_0}{(1+\frac{r^2}{a^2})^{\frac{\gamma+1}{2}}} \qquad (1)$$

We estimated the central mass density of $\rho_0 = (3.80^{+1.57}_{-1.11}) \times 10^4\,[{\rm M}_\odot\,{\rm pc}^{-2}]$, $\rho_0 = (2.51^{+0.72}_{-0.56}) \times 10^4\,[{\rm M}_\odot\,{\rm pc}^{-2}]$, and $\rho_0 = (2.24^{+0.58}_{-0.46}) \times 10^4 [{\rm M}_\odot\,{\rm pc}^{-2}]$, at the ages of 1, 1.5, and 2 Myr, respectively. The central density at 1 Myr is higher than the other ages because most of the massive stars are located at the central part of the cluster [see Fig. 9 (middle)], and for these stars, the stellar mass estimation is higher at lower ages.

The total mass of the cluster ($M_{\rm tot}$) and the cluster's surface density (Σ), which is the projected mass density within a given radius, i.e. all the mass between 0 and r divided by the area of the corresponding circle, are shown in Fig. 12. Σ and $M_{\rm tot}$ become consistent at different ages for larger radii (starting at 0.3 pc up to 1.3 pc), where lots of pre-main-sequence and low-mass stars are located/detected. The surface density of R136 at $R = 0.3$pc (and $R_{\rm max} = 1.3$pc) reaches to $1.4^{+0.7}_{0.4} \times 10^4\,[{\rm M}_\odot\,{\rm pc}^{-2}]$ (and $2.7^{+1.1}_{0.6} \times 10^3\,[{\rm M}_\odot\,{\rm pc}^{-2}]$), and the total mass down to $1.0 \pm 0.1\,{\rm M}_\odot$ is $4.0^{+1.7}_{-1.2} \times 10^3\,{\rm M}_\odot$ (and $1.5^{+0.5}_{-0.4} \times 10^4\,{\rm M}_\odot$), respectively.

[12]The reported values are consistent for ones derived without completeness correction. To compare these plots w/o completeness at 1.5 Myr, see Fig. A6.

Downloaded from https://academic.oup.com/mnras/article/503/1/292/6133467 by CNRS - ISTO user on 07 June 2022

The densities and total estimated masses at 1 Myr are slightly higher than the values reported in the first epoch [compare Fig. 12 to fig. 13 in Khorrami et al. (2017)].

Fitted γ and a parameters (in equation 1) vary from 0.8 to 0.85 and 0.14 to 0.19, respectively, depending on the selected age.

Comparing these values to the previous ones estimated for 818 stars in the 2015 data in J–K data (Khorrami et al. 2017), ρ_0 and a are consistent within the given errors to their previous values of $\rho_0 = (3.89^{+1.60}_{-1.14}) \times 10^4 [M_\odot\,pc^{-2}]$ and $a = 0.17 \pm 0.05$, but γ is decreased by about 0.4.

7 JHK COLOURS

Among 818 sources detected in J and K in 2015 data, and 1499 sources detected in H and K in 2018, we could detect 790 sources common in total (J, H, and K). 30 per cent of the newly detected sources in 2018 had enough SNR to be detected in the K data in 2015 (they are brighter than the faintest star in the 2015 K catalogue), but these sources were not listed in the J since the AO correction for J data is not as good as in K. These sources were located either in the central part of the cluster where AO halo (uncorrected part of the stellar signal with the FWHM of seeing) was large leading to decreasing their SNR or in the outer part of the cluster where the PSF was distorted [see photometric selection criteria in Khorrami et al. (2017)] due to anisoplanatism.

For these 790 common sources between two epochs, we have plotted colour–colour diagram in (J–K) versus (H–K) for 413 stars in the central region $r < 3''$ (Fig. 13 top) and 377 sources in the outer region $r > 3''$ [Fig. 13 (bottom)]. The black circles in Fig. 13 show 49 stars studied by Bestenlehner et al. (2020) in the centre of R136, and the black solid line is the PARSEC isochrone at 2 Myr. These plots show that the detected sources in the inner region of R136 are more consistent with the evolutionary models than the sources in the outer region of the cluster. Comparing the CMD in H–K and J–K (Fig. 9) for inner and outer regions, the dispersion in the colour of the detected sources in the outer region is higher than in the inner region. In the first epoch, 48 per cent of the detected sources in J and K were in the outer region, but in the second epoch, this number increases to 58 per cent. Only about 30 per cent (70 per cent) of the new detected sources in the second epoch (H–K) are located in the inner (outer) region. This can be explained by the effect of incompleteness in the core, so that even with the longer exposure time and better observing condition (e.g. SR > 70 per cent), central region remains too bright for low-mass MS stars to be detected. The completeness in H and K, for the central region of R136, is less than 50 per cent (20 per cent) for the magnitude range of 19–20 (20–21) in our completeness maps (Fig. A1).

8 CONCLUSIONS

We presented a new photometric analysis of the core of R136 using the second epoch data from VLT/SPHERE instrument in the near-IR. We observed R136 in H and K filters in better atmospheric observing conditions and longer exposure time than the first epoch. This enabled us to detect twice as many sources (in H and K) as we have detected in the first epoch (in J and K) in the FOV of IRDIS ($10.8'' \times 12.1''$) covering almost 2.7×3.0 pc of R136 core. Among 1658 and 2528 detected sources in H and K, respectively, we found 1499 common sources between these two sets of data, where 76 per cent of these sources have visual companion closer than $0.2''$, which is higher than the value found in the first epoch in 2015 data (Khorrami et al. 2017). About 71 per cent of the newly detected sources are located in the outer region ($r > 3''$) of the cluster.

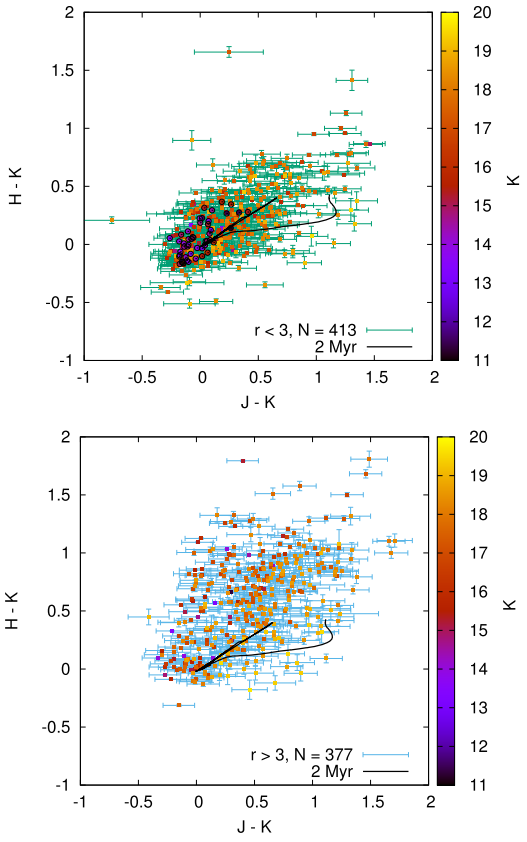


Figure 13. Colour–colour diagram for the common sources between J, H, and K, within two epochs J–K (2015) and H–K (2018), for the central region $r < 3''$ (top) and outer region $r > 3''$ (bottom). The colour indicates the K magnitude of detected sources and the black circles represent 49 stars studied by Bestenlehner et al. (2020) listed in Table A1. The black solid line is the PARSEC isochrone at 2 Myr with $E(H-K) = 0.1$ and $E(J-K) = 0.25$. The right-hand side of the curve represents pre-main-sequence part of isochrone, followed by the main-sequence locus on the straight line on the centre and the post-main-sequence part on the top.

Using the stellar parameters (*Teff*, log g, and logL) of 49 stars studied spectroscopically by Bestenlehner et al. (2020) in the optical, PARSEC isochrones, TLUSTY SEDs (Hubeny & Lanz 1995; Lanz & Hubeny 2003), and synthetic extinction curves from Draine (2003a, 2003b, 2003c), Li & Draine (2001), and Weingartner & Draine (2001), we estimated the extinction at DM of 18.49 magnitude, using two methods (Section 6). We adopt the extinctions of $A_H = 0.45$ and $A_K = 0.35$ magnitudes, which are consistent with the two methods (within the error bars) and De Marchi & Panagia (2014). The colour excess of $E(H-K) = 0.1$ is also consistent with Tatton et al. (2013) and with the one used in previous studies by Campbell et al. (2010). Consequently, the stellar masses were calculated at the ages of 1.0, 1.5, and 2.0 Myr.

The MF slope for 1, 1.5, and 2 Myr isochrone at the inner ($r < 3''$) and outer regions ($r > 3''$) of the cluster is estimated and shown in Table 3. One can check the effect of incompleteness by comparing the MF slopes before and after the completeness correction, shown as Γ_{NC} and Γ_{CC}, respectively, in Table 3. The completeness-corrected MF slopes for the whole FOV ($\Gamma_{1Myr} = -0.93 \pm 0.08$, $\Gamma_{1.5Myr} = -0.98 \pm 0.09$) are consistent with the values derived from the photometric analysis of the first epoch data (Khorrami et al. 2017) for the mass range of 3–300 $M_\odot$ ($\Gamma_{1Myr} = -0.90 \pm 0.13$, $\Gamma_{1.5Myr} =$

Downloaded from https://academic.oup.com/mnras/article/503/1/292/6133467 by CNRS - ISTO user on 07 June 2022

-0.98 ± 0.18) and are closer to the Salpeter value (Salpeter 1955) for the high mass range of 10–300 $M_\odot$ ($\Gamma_{1.5Myr} = -1.26 \pm 0.01$, $\Gamma_{2Myr} = -1.34 \pm 0.03$). The MF slopes for the mass range of 10–300 $M_\odot$ are about 0.3 dex steeper than the mass range of 3–300 $M_\odot$, for the whole FOV and for different radii. The MF slopes in the inner region are shallower than in the outer region for different mass ranges. In Fig. 11, Λ_{MSR} with a value (about 2 sigma) above 1 shows a degree of mass segregation. Considering the spatial distribution of completeness (Fig. A1), both MF slope in the core and Λ_{MSR} would decrease, if the number of low-mass stars increases in the centre where the completeness is very low.

We corrected the MF for completeness for sources fainter than 17 mag (1226 stars in the whole FOV and 444/782 stars in inner/outer region). Still these values are low limits to the steepness due to incompleteness and central concentration of bright stars.

The surface density of R136 at $R = 0.3$ pc (and $R_{max} = 1.3$ pc) reaches to $1.4^{+0.7}_{0.4} \times 10^4$ [$M_\odot$ pc^{-2}] (and $2.7^{+1.1}_{0.6} \times 10^3$ [$M_\odot$ pc^{-2}]), and the total mass down to 1.0 ± 0.1 $M_\odot$ is $4.0^{+1.7}_{-1.2} \times 10^3$ $M_\odot$ (and $1.5^{+0.5}_{-0.4} \times 10^4$ $M_\odot$), respectively. The densities and total estimated masses at 1 Myr are slightly higher than the values reported in the first epoch [compare Fig. 12 to fig. 13 in Khorrami et al. (2017)].

Comparing data with the first epoch ones, we could detect 790 sources common in total (J, H, and K) and the majority (67 per cent) of detected sources in the outer region ($r > 3''$) are not consistent with the evolutionary models at 1−2 Myr and with extinction similar to the average cluster value, suggesting an ongoing star formation within 30 Doradus. A significant scatter in the CMD (Fig. 9) and colour–colour diagram (Fig. 13) is originated mainly from the lower part of the main-sequence and pre-main-sequence sources, located (detected) at the outer region. The observed scatter in CMD and colour–colour diagrams of 30 Doradus has previously been reported in the visible and NIR (Hunter et al. 1995; Andersen et al. 2009; De Marchi et al. 2011; Cignoni et al. 2015). The scatter is likely due to a combination of observational confusion (affected mainly by the visual multiple systems or variables), photometric errors, differential extinction, and a possible age spread. In addition, pre-main-sequence stars are often associated with circumstellar discs and outflows, which will introduce additional extinction for the cluster's low-mass content. Brandl et al. (1996) found that the extinction varies significantly from star to star within the cluster, with the range of 1–2 mag. The *HST* observations also reveal the presence of considerable differential extinction across the 30 Doradus region. De Marchi et al. (2011) quantified the total extinction towards massive main-sequence stars younger than 3 Myr to be in the range of $1.3 < A_V < 2.1$.

This motivates us to observe this cluster again in J and K in future with even longer exposure time, so the number of common sources in three filters (J, H, and K) increases.

ACKNOWLEDGEMENTS

The Star Form Mapper project has received funding from the European Union's Horizon 2020 research and innovation program under grant agreement no. 687528. Zeinab Khorrami acknowledges the support of a STFC Consolidated Grant (ST/K00926/1). This work has made use of the SPHERE Data Centre, jointly operated by OSUG/IPAG (Grenoble), PYTHEAS/LAM/CeSAM (Marseille), OCA/Lagrange (Nice), Observatoire de Paris/LESIA (Paris), and Observatoire de Lyon (OSUL/CRAL). This work is supported by the French National Programmes (PNPS). Anne Buckner is funded by the European Research Council H2020-EU.1.1 ICYBOB project (grant no. 818940). Richard Wünsch and Jan Palouš acknowledge support by the Czech Science Foundation project no. 19-15008S and by the institutional project RVO:67985815.

Based on observations made with ESO Telescopes at the La Silla Paranal Observatory, under programme ID 0102.D0271.

DATA AVAILABILITY

All data are incorporated into the article and its online supplementary material.

REFERENCES

Allison R. J., Goodwin S. P., Parker R. J., Portegies Zwart S. F., de Grijs R., Kouwenhoven M. B. N., 2009, MNRAS, 395, 1449
Andersen M., Zinnecker H., Moneti A., McCaughrean M. J., Brandl B., Brandner W., Meylan G., Hunter D., 2009, ApJ, 707, 1347
Bestenlehner J. M. et al., 2014, A&A, 570, A38
Bestenlehner J. M. et al., 2020, MNRAS, 499, 1918
Beuzit J. L. et al., 2019, A&A, 631, A155
Brandl B. et al., 1996, ApJ, 466, 254
Bressan A., Marigo P., Girardi L., Salasnich B., Dal Cero C., Rubele S., Nanni A., 2012, MNRAS, 427, 127
Campbell M. A., Evans C. J., Mackey A. D., Gieles M., Alves J., Ascenso J., Bastian N., Longmore A. J., 2010, MNRAS, 405, 421
Chen Y. et al., 2019, A&A, 632, A105
Cignoni M. et al., 2015, ApJ, 811, 76
Crowther P. A., Dessart L., 1998, MNRAS, 296, 622
Crowther P. A., Schnurr O., Hirschi R., Yusof N., Parker R. J., Goodwin S. P., Kassim H. A., 2010, MNRAS, 408, 731
Crowther P. A. et al., 2016, MNRAS, 458, 624
De Marchi G., Panagia N., 2014, MNRAS, 445, 93
De Marchi G. et al., 2011, ApJ, 739, 27
Diolaiti E., Bendinelli O., Bonaccini D., Close L., Currie D., Parmeggiani G., 2000, A&AS, 147, 335
Draine B. T., 2003a, ARA&A, 41, 241
Draine B. T., 2003b, ApJ, 598, 1017
Draine B. T., 2003c, ApJ, 598, 1026
Elson R. A. W., Fall S. M., Freeman K. C., 1987, ApJ, 323, 54
Fusco T. et al., 2004, J. Opt. A: Pure Appl. Opt., 6, 585
Gibson B. K., 2000, MemSAI, 71, 693
Guerrero M. A., Chu Y.-H., 2008, ApJS, 177, 216
Hubeny I., Lanz T., 1995, ApJ, 439, 875
Hunter D. A., Shaya E. J., Holtzman J. A., 1995, ApJ, 448, 179
Khorrami Z. et al., 2017, A&A, 602, A56
Khorrami Z. et al., 2019, MNRAS, 485, 3124
Langlois M. et al., 2014, in Ramsay S. K., McLean I. S., Takami H., eds, Proc. SPIE Conf. Ser. Vol. 9147, Ground-based and Airborne Instrumentation for Astronomy V. SPIE, Bellingham, p. 91471R
Lanz T., Hubeny I., 2003, ApJS, 147, 225
Li A., Draine B. T., 2001, ApJ, 554, 778
Maire A.-L. et al., 2014, A&A, 566, A126
Massey P., Hunter D. A., 1998, ApJ, 493, 180
Pietrzyński G. et al., 2013, NAT, 495, 76
Portegies Zwart S. F., Pooley D., Lewin W. H. G., 2002, ApJ, 574, 762
Pugliese G., Christou J., Koehler R., Drummond J., 2002, BAAS, 34, 55.05
Salpeter E. E., 1955, ApJ, 121, 161
Schneider F. R. N. et al., 2018, A&A, 618, A73
Schnurr O., Chené A. -N., Casoli J., Moffat A. F. J., St-Louis N., 2009, MNRAS, 397, 2049
Tatton B. L. et al., 2013, A&A, 554, A33
Townsley L. K., Broos P. S., Feigelson E. D., Garmire G. P., Getman K. V., 2006, AJ, 131, 2164
Weigelt G., Baier G., 1985, A&A, 150, L18
Weingartner J. C., Draine B. T., 2001, ApJ, 548, 296

Downloaded from https://academic.oup.com/mnras/article/503/1/292/6133467 by CNRS - ISTO user on 07 June 2022

SUPPORTING INFORMATION

Supplementary data are available at *MNRAS* online.

Table A3. Sample catalogue of detected sources in H and K data in 2018.

Please note: Oxford University Press is not responsible for the content or functionality of any supporting materials supplied by the authors. Any queries (other than missing material) should be directed to the corresponding author for the article.

APPENDIX A: ADDITIONAL TABLE AND FIGURES

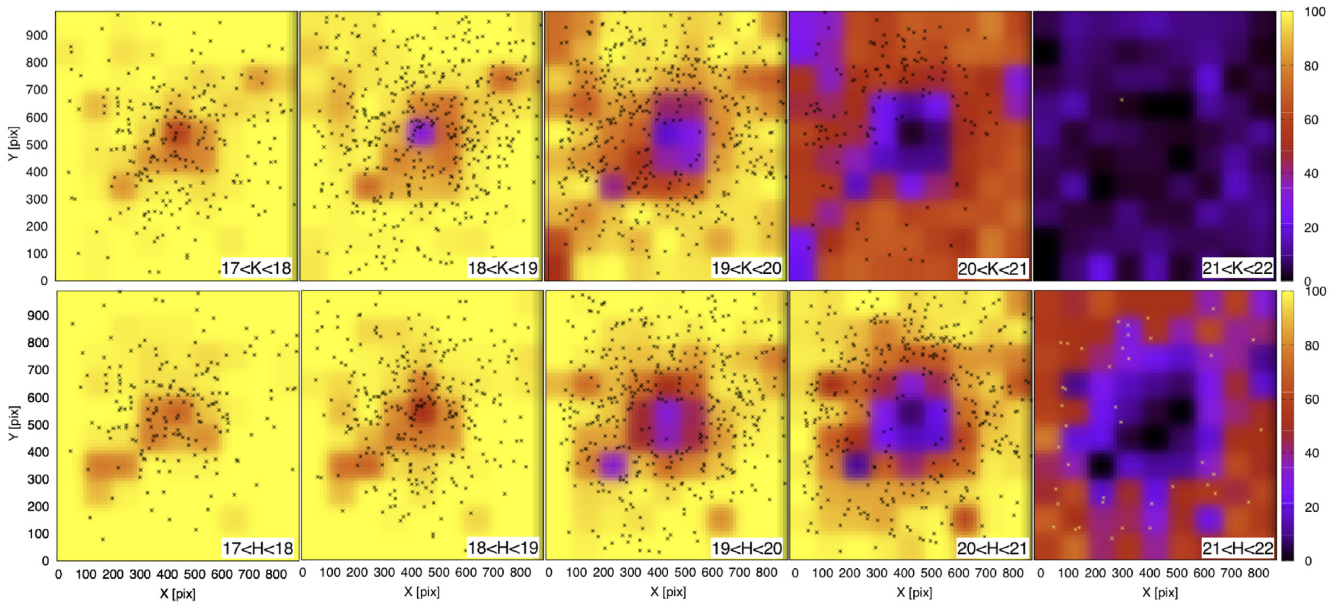


Figure A1. Completeness maps in K (top) and H (bottom), used for correcting stellar masses for plotting MF. Colour range (0:100). Stars show the location of the observed detected sources within the given magnitude range for each map. If a star with a given magnitude is located in the yellow area, it will be detected 100 per cent and it has difficulty to be detected if it is located in the dark purple.

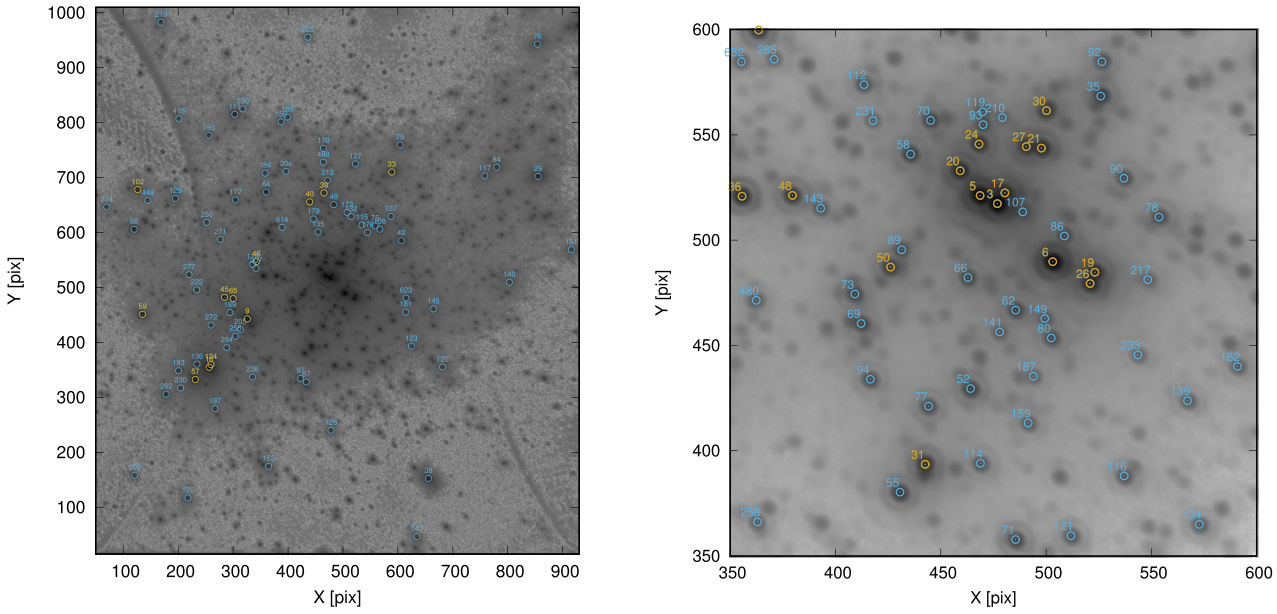


Figure A2. Stars brighter than 16 mag (14 mag) in K data shown in blue circles (yellow), with HSH95 identification written on top of each source. See Table A2 for their IRIDS (J, H, and K) and *HST* (U, V, and I) magnitudes. Left: Whole FOV, Right: Same as left but zoomed in the core to avoid confusion. Background image is the SPHERE/IRDIS/K in 2018.

Downloaded from https://academic.oup.com/mnras/article/503/1/292/6133467 by CNRS - ISTO user on 07 June 2022

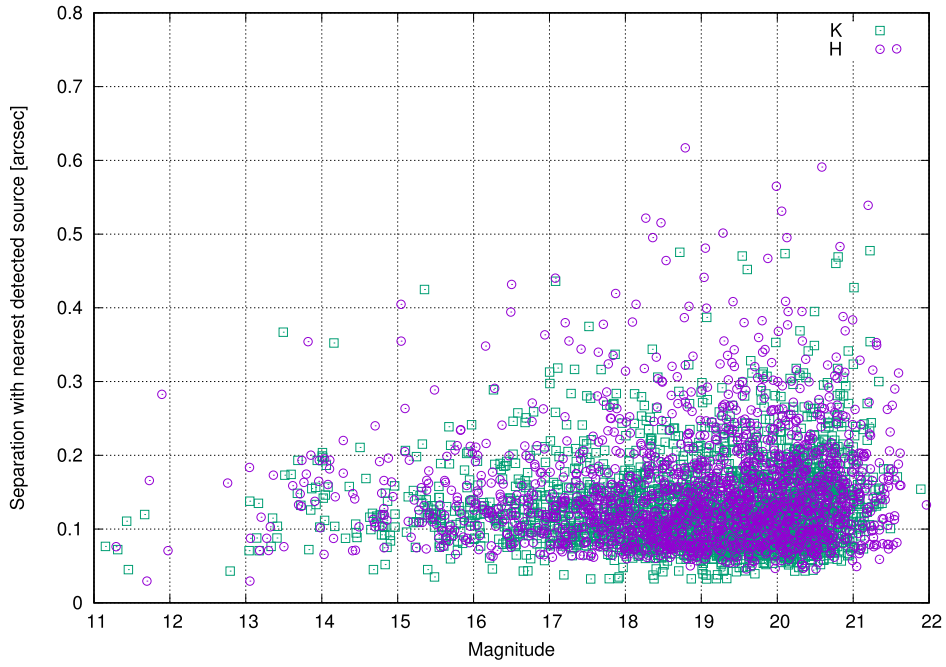


Figure A3. Separation from the nearest neighbour for each detected sources in H (purple circles) and K (green squares) versus their magnitudes.

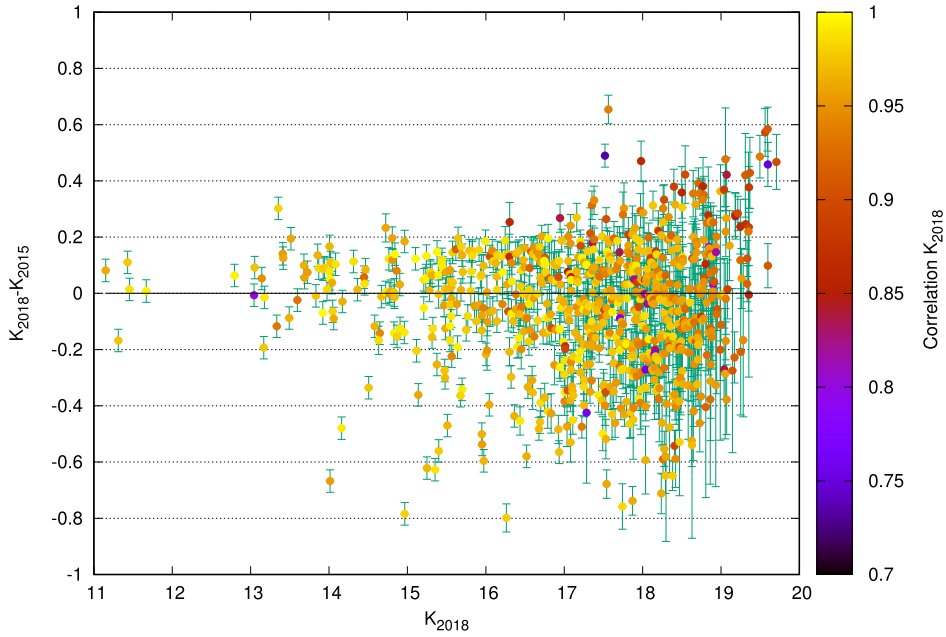


Figure A4. Difference between the K magnitude of the sources within two epochs versus their K magnitude in 2018. The colour shows the correlation between the detected source and the input PSF. The higher the value, the more similar the shape of PSF is to the reference input PSF.

Downloaded from https://academic.oup.com/mnras/article/503/1/292/6133467 by CNRS - ISTO user on 07 June 2022

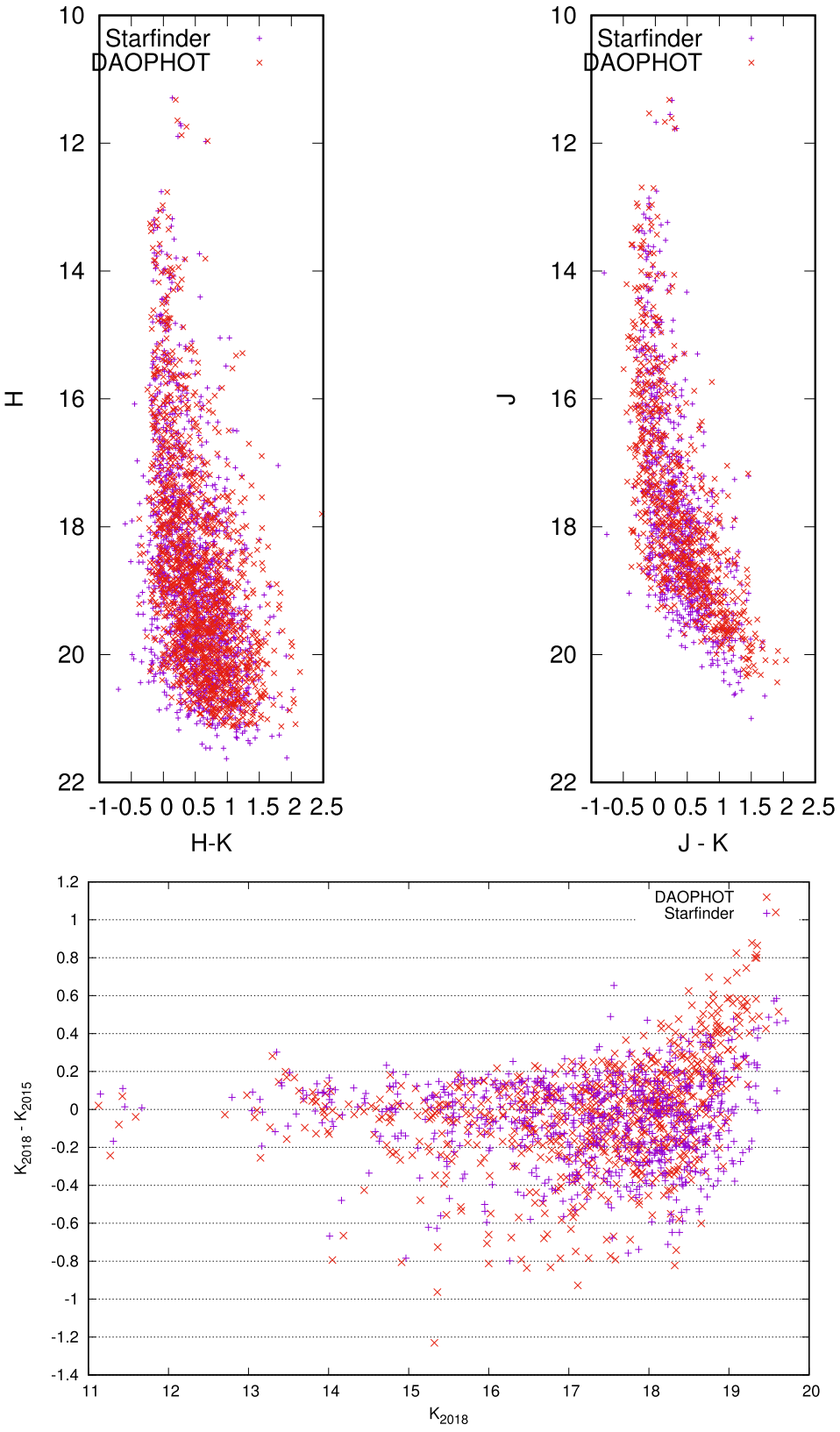


Figure A5. Comparing the photometry by *Starfinder* (purple crosses) with DAOPHOT (red pluses). Top show the CMD in H–K in 2018 data (left) and J–K in 2015 (right). Bottom is the comparison between the K magnitude of common sources between two epochs.

Downloaded from https://academic.oup.com/mnras/article/503/1/292/6133467 by CNRS - ISTO user on 07 June 2022

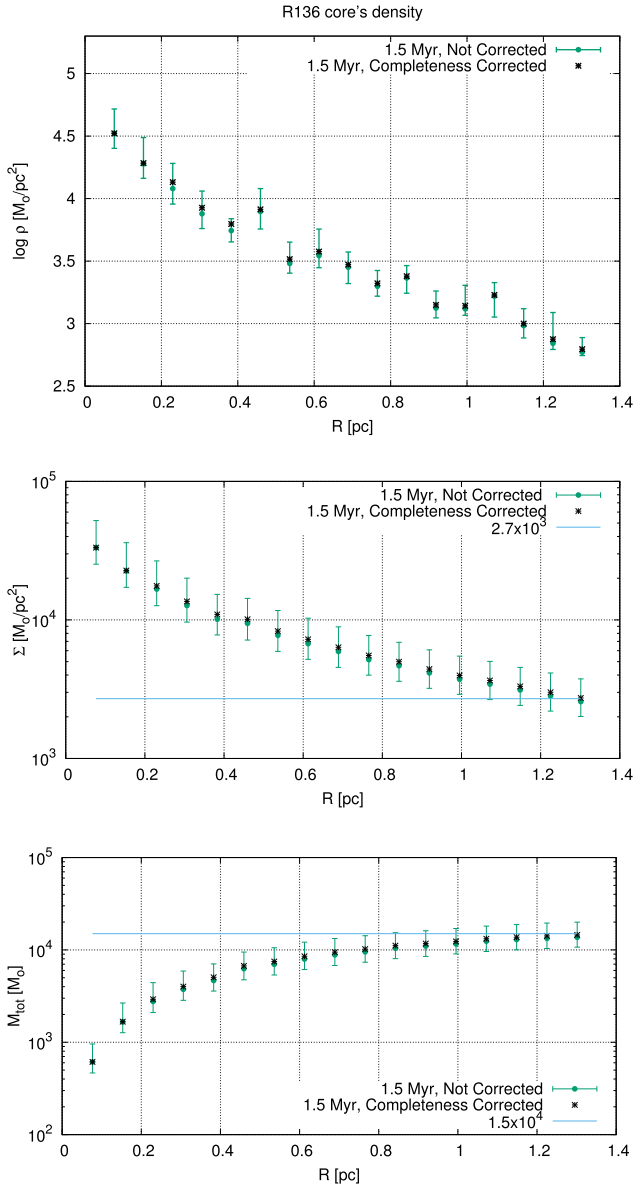


Figure A6. Comparing the effect of completeness correction on the density of the cluster at 1.5 Myr. Same as Fig. 12 for 1.5 Myr. Black stars are the completeness-corrected values.

Downloaded from https://academic.oup.com/mnras/article/503/1/292/6133467 by CNRS - ISTO user on 07 June 2022

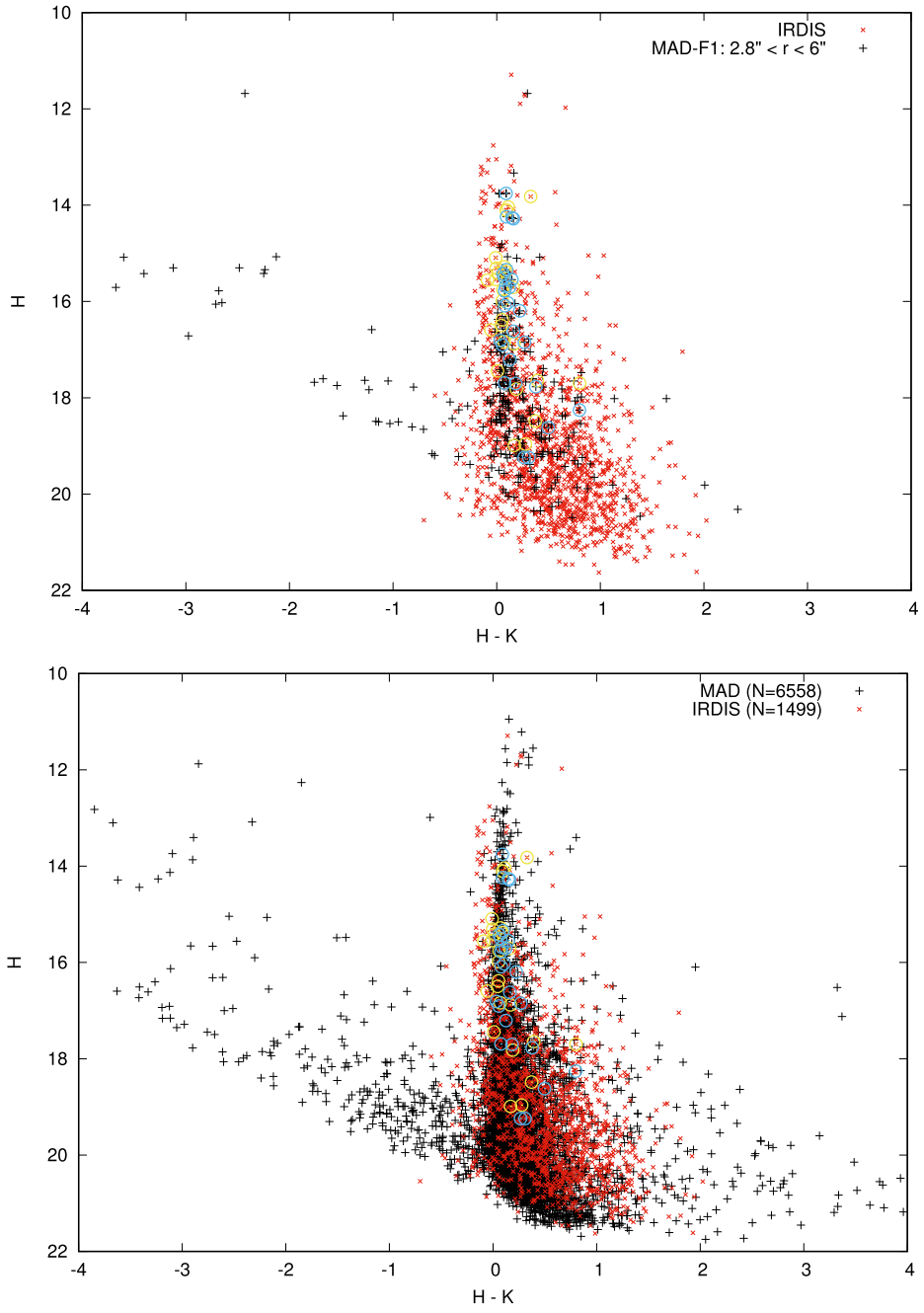


Figure A7. Comparing H–K CMD between IRDIS (this work, red crosses) and MAD [Campbell et al. (2010), black pluses]. Top shows the MAD data within the same FOV of IRDIS (2.8″ excluded), and bottom shows the whole MAD data covering F1-F2-F3. Yellow and blue circles show the 28 common sources used for adjusting zero-points. The number of common sources between IRDIS FOV and MAD catalogue is larger than 26, but since both our catalogues have pix position for the location of stars, we needed to identify stars by eye in each image/catalogue.

Downloaded from https://academic.oup.com/mnras/article/503/1/292/6133467 by CNRS - ISTO user on 07 June 2022

Table A1. List of brightest spectroscopically known stars in the core of R136 studied in optical. $T_{\rm eff}$, log L/L$_\odot$, and log g, and spectral types are taken from Bestenlehner et al. 2020 (Table 1). Ones noted in brackets, [MH98], [CD98], [C10], [B14], and [C16] are from Massey & Hunter (1998), Crowther & Dessart (1998), Crowther et al. (2010), Bestenlehner et al. (2014), and Crowther et al. (2016), respectively. HSH95, WB85, and ID$_{\rm K}$ are the stars' identification in Hunter et al. (1995), Weigelt & Baier (1985), and SPHERE/IRDIS/K catalogue in 2018 (this work), respectively. K and H are the SPHERE IRDIS magnitudes and J$_{15}$ is the SPHERE IRDIS magnitude in our first epoch data (Khorrami et al. 2017). r is the distance from r136a1 in our K data. The stellar initial masses ($M_{\rm ini}$) and ages are estimated by fitting grids of PARSEC evolutionary models (0.1–10 Myr) to the $T_{\rm eff}$ and log L/L$_\odot$.

HSH95 (WB85)	ID$_K$	K($\pm$ 0.01) (mag)	H($\pm$ 0.01) (mag)	J$_{15}$($\pm$ 0.13) (mag)	r (arcsec)	$T_{\rm eff}$ (kK)	log L/L$_\odot$	log g	$M_{\rm ini}$ (M$_\odot$)	Age (Myr)	Spectral type
3 (a1)	1	11.15	11.29	11.33	0.00	46.0 $\pm$ 2.5	$6.79^{+0.10}_{-0.10}$	4.0	207^{+142}_{-28}	$2.4^{+0.1}_{-1.5}$	WN5h [CD98]
10 (c)	2	11.31	11.70	11.78	3.35	42.0 $\pm$ 2.0 [B14]	6.58 $\pm$ 0.10 [B14]	–	–	–	WN5h [C10]
5 (a2)	3	11.43	11.70	11.55	0.11	50.0 $\pm$ 2.5	$6.75^{+0.10}_{-0.10}$	4.0	202^{+147}_{-26}	$2.4^{+0.1}_{-1.8}$	WN5h [CD98]
6 (a3)	4	11.45	11.73	11.77	0.47	50.0 $\pm$ 2.5	$6.63^{+0.10}_{-0.10}$	4.0	200^{+50}_{-45}	$0.9^{+1.7}_{-0.3}$	WN5h [CD98]
9 (b)	5	11.67	11.90	11.67	2.06	35.0 $\pm$ 2.5	$6.34^{+0.12}_{-0.10}$	3.3	102^{+36}_{-23}	$3.0^{+0.4}_{-1.1}$	O4If/WN8 [C16]
20 (a5)	6	12.79	12.76	12.75	0.29	47.0 $\pm$ 3.3	$6.29^{+0.10}_{-0.09}$	4.0	120^{+19}_{-45}	$1.3^{+2.2}_{-0.2}$	O2I(n)f*
19 (a6)	11	13.17	13.30	13.28	0.71	53.0 $\pm$ 3.5	$6.27^{+0.09}_{-0.09}$	4.1	121^{+12}_{-46}	$0.7^{+2.8}_{-0.6}$	O2I(n)f*p
36	8	13.05	13.05	12.86	1.49	52.0 $\pm$ 3.4	$6.33^{+0.12}_{-0.10}$	4.1	130^{+19}_{-50}	$0.8^{+2.6}_{-0.7}$	O2If*
21 (a4)	9	13.14	13.06	13.00	0.41	48.0 $\pm$ 5.8	$6.24^{+0.18}_{-0.18}$	4.1	110^{+39}_{-51}	$1.4^{+2.7}_{-1.2}$	O3V((f*))(n)
24 (a7)	13	13.35	13.20	12.95	0.36	49.0 $\pm$ 5.5	$6.25^{+0.18}_{-0.17}$	4.2	112^{+37}_{-48}	$1.3^{+2.6}_{-1.2}$	O3III(f*) [MH98]
46	15	13.42	13.32	13.11	1.69	49.0 $\pm$ 6.0	$6.16^{+0.18}_{-0.17}$	4.2	100^{+30}_{-46}	$1.2^{+3.2}_{-1.1}$	O2-3III(f*)
47	17	13.51	13.36	13.17	1.72	47.0 $\pm$ 7.0	$6.09^{+0.22}_{-0.21}$	4.0	90^{+30}_{-36}	$1.4^{+3.0}_{-1.3}$	O2V((f*))
31	18	13.60	13.80	13.69	1.57	48.0 $\pm$ 5.0	$6.01^{+0.16}_{-0.16}$	4.0	80^{+20}_{-26}	$1.4^{+3.0}_{-1.3}$	O2V((f*))
48	19	13.68	13.62	13.41	1.19	49.0 $\pm$ 7.2	$6.05^{+0.21}_{-0.20}$	4.1	83^{+36}_{-29}	$1.5^{+2.9}_{-1.4}$	O2-3III(f*)
45	20	13.69	13.74	13.37	2.39	42.0 $\pm$ 5.0	$5.84^{+0.17}_{-0.16}$	3.9	59^{+15}_{-13}	$2.5^{+1.9}_{-1.0}$	O4:Vz
30	21	13.73	13.69	13.62	0.61	37.0 $\pm$ 3.5	$5.68^{+0.14}_{-0.14}$	3.9	45^{+10}_{-7}	$3.6^{+0.8}_{-0.7}$	O6.5Vz
40	23	13.86	13.72	13.61	1.76	45.0 $\pm$ 5.6	$5.88^{+0.18}_{-0.18}$	3.9	65^{+20}_{-15}	$2.0^{+2.4}_{-1.9}$	O3V
65	27	13.94	13.97	13.67	2.21	42.0 $\pm$ 5.2	$5.74^{+0.17}_{-0.16}$	4.0	51^{+15}_{-11}	$2.8^{+1.0}_{-1.9}$	O4 V [C16]
50	28	13.97	13.98	13.82	0.72	42.0 $\pm$ 3.0	$5.71^{+0.11}_{-0.11}$	3.8	50^{+7}_{-7}	$2.7^{+0.7}_{-0.7}$	O3-4 V((f*))
64	29	14.01	13.86	13.69	2.39	40.0 $\pm$ 5.1	$5.69^{+0.18}_{-0.17}$	3.9	47^{+14}_{-10}	$3.0^{+1.3}_{-1.3}$	O4-5V
58	33	14.02	13.91	13.78	0.58	50.0 $\pm$ 5.9	$5.94^{+0.16}_{-0.16}$	4.1	75^{+22}_{-21}	$1.0^{+3.4}_{-0.9}$	O2-3V
35	34	14.04	14.03	14.04	0.87	44.0 $\pm$ 5.6	$5.74^{+0.18}_{-0.18}$	4.0	53^{+0}_{-0}	$2.3^{+0.0}_{-0.0}$	O3V
55	36	14.06	14.28	14.15	1.77	47.0 $\pm$ 5.0	$5.76^{+0.15}_{-0.15}$	3.9	57^{+17}_{-12}	$1.5^{+1.3}_{-1.4}$	O2V((f*))z
49	37	14.08	13.96	13.94	1.64	48.0 $\pm$ 12.0	$5.89^{+0.37}_{-0.37}$	4.2	68^{+51}_{-30}	$1.5^{+3.0}_{-1.4}$	O3V [MH98]
52	39	14.17	14.28	14.10	1.09	44.0 $\pm$ 4.8	$5.67^{+0.16}_{-0.16}$	4.0	50^{+11}_{-10}	$2.2^{+1.3}_{-2.1}$	O3-4Vz
70	40	14.31	14.16	14.06	0.62	47.0 $\pm$ 6.0	$5.78^{+0.18}_{-0.18}$	4.2	60^{+20}_{-15}	$1.4^{+1.6}_{-1.3}$	O5Vz
62	41	14.36	14.41	14.28	0.63	49.0 $\pm$ 6.2	$5.75^{+0.17}_{-0.17}$	4.0	60^{+15}_{-15}	$0.8^{+1.8}_{-0.7}$	O2-3V
69	42	14.45	14.49	14.29	1.06	41.0 $\pm$ 4.6	$5.51^{+0.16}_{-0.16}$	4.1	40^{+10}_{-8}	$3.0^{+1.4}_{-2.8}$	O4-5Vz
66	43	14.45	14.44	14.31	0.46	46.0 $\pm$ 6.6	$5.64^{+0.21}_{-0.21}$	4.1	50^{+20}_{-13}	$1.7^{+1.8}_{-1.6}$	O2V-III(f*)
73	44	14.46	14.44	14.24	0.98	33.0 $\pm$ 3.6	$5.27^{+0.14}_{-0.14}$	4.3	27^{+4}_{-4}	$5.6^{+2.0}_{-1.1}$	O9.7-B0V
71	46	14.58	14.88	14.80	1.96	48.0 $\pm$ 8.0	$5.56^{+0.23}_{-0.23}$	3.9	50^{+15}_{-16}	$0.2^{+3.2}_{-0.1}$	O2-3V((f*))
86	47	14.63	14.82	14.80	0.43	41.0 $\pm$ 5.0	$5.26^{+0.16}_{-0.16}$	3.8	31^{+10}_{-5}	$3.1^{+1.9}_{-3.0}$	O5:V
78	49	14.67	14.76	14.76	0.94	48.0 $\pm$ 8.0	$5.60^{+0.24}_{-0.24}$	4.2	50^{+20}_{-15}	$0.9^{+2.5}_{-0.8}$	O4:V
80	54	14.77	14.83	14.71	0.84	35.0 $\pm$ 3.8	$5.15^{+0.15}_{-0.15}$	3.8	25^{+4}_{-4}	$5.3^{+1.9}_{-2.3}$	O8V
75	55	14.79	14.82	14.84	1.53	39.0 $\pm$ 6.9	$5.29^{+0.22}_{-0.22}$	4.3	31^{+11}_{-8}	$3.7^{+2.9}_{-3.6}$	O6V
90	59	14.83	14.86	14.88	0.75	40.0 $\pm$ 3.7	$5.32^{+0.13}_{-0.13}$	4.1	32^{+7}_{-5}	$3.4^{+1.4}_{-2.9}$	O4:V:
94	60	14.84	14.92	14.69	1.26	48.0 $\pm$ 8.2	$5.52^{+0.23}_{-0.23}$	4.2	47^{+12}_{-15}	$0.3^{+3.1}_{-0.2}$	O4-5Vz
129	61	14.84	14.79	14.43	0.97	37.0 $\pm$ 8.2	$4.37^{+0.26}_{-0.26}$	4.0	–	–	–
92	64	14.90	14.94	14.96	1.02	39.0 $\pm$ 4.0	$5.26^{+0.14}_{-0.14}$	4.0	30^{+6}_{-4}	$3.9^{+1.5}_{-3.2}$	O6Vz
112	67	14.96	14.80	14.61	1.04	36.0 $\pm$ 6.0	$5.21^{+0.19}_{-0.19}$	4.3	27^{+8}_{-6}	$5.0^{+2.7}_{-4.6}$	O7-9Vz
114	72	15.21	15.38	15.33	1.51	44.0 $\pm$ 6.8	$5.25^{+0.21}_{-0.21}$	4.2	35^{+8}_{-9}	$0.7^{+3.7}_{-0.6}$	O5-6V
143	75	15.24	15.14	14.93	1.03	39.0 $\pm$ 6.0	$5.18^{+0.20}_{-0.20}$	4.2	28^{+9}_{-7}	$3.3^{+3.2}_{-3.2}$	O8-9 V-III
121	81	15.31	15.63	15.50	1.98	34.0 $\pm$ 4.8	$4.86^{+0.16}_{-0.16}$	4.2	20^{+5}_{-3}	$6.3^{+3.5}_{-5.7}$	O9.5V
116	82	15.32	15.60	15.86	1.75	34.0 $\pm$ 6.1	$4.84^{+0.16}_{-0.16}$	3.7	20^{+5}_{-3}	$5.9^{+3.5}_{-5.8}$	O7V
141	87	15.40	15.46	15.33	0.75	32.0 $\pm$ 6.0	$4.79^{+0.21}_{-0.21}$	3.6	18^{+5}_{-2}	$7.8^{+2.2}_{-7.7}$	O5-6V [C16]
135	90	15.44	15.28	15.17	1.06	33.0 $\pm$ 4.9	$4.89^{+0.17}_{-0.17}$	4.0	20^{+5}_{-3}	$6.9^{+3.1}_{-6.3}$	B

Downloaded from https://academic.oup.com/mnras/article/503/1/292/6133467 by CNRS - ISTO user on 07 June 2022

Table A1 – *continued*

HSH95 (WB85)	ID_K	K(± 0.01) (mag)	H(± 0.01) (mag)	J_{15}(± 0.13) (mag)	r (arcsec)	$T_{\rm eff}$ (kK)	log $L/L_\odot$	log g	$M_{\rm ini}$ ($M_\odot$)	Age (Myr)	Spectral type
132	91	15.45	15.35	15.38	1.45	39.0 ± 5.8	$5.05^{+0.20}_{-0.20}$	4.0	26^{+8}_{-6}	$3.1^{+3.5}_{-3.0}$	O7:V
159	92	15.47	15.62	15.51	0.32	36.0 ± 8.9	$4.93^{+0.28}_{-0.28}$	4.3	–	–	–
120	93	15.48	16.05	16.11	0.80	37.0 ± 6.8	$4.81^{+0.22}_{-0.22}$	4.3	–	–	–
123	95	15.49	15.83	15.88	2.36	41.0 ± 6.5	$5.01^{+0.22}_{-0.22}$	4.1	28^{+7}_{-8}	$0.4^{+5.4}_{-0.3}$	O6V
134	99	15.54	15.91	15.90	2.21	36.0 ± 4.8	$4.81^{+0.17}_{-0.17}$	4.0	20^{+4}_{-4}	$3.9^{+4.4}_{-3.8}$	O7Vz
162	101	15.54	15.78	15.98	0.42	37.0 ± 13.0	$4.87^{+0.39}_{-0.39}$	4.3	–	–	–
108	102	15.55	15.57	15.71	1.55	43.0 ± 7.6	$5.04^{+0.24}_{-0.24}$	4.2	28^{+6}_{-7}	$0.7^{+4.6}_{-0.6}$	OVn
139	105	15.56	15.78	15.72	0.40	38.0 ± 5.1	$4.90^{+0.17}_{-0.17}$	4.0	–	–	–
173	121	15.71	15.63	15.70	1.51	30.0 ± 10.0	$4.65^{+0.33}_{-0.33}$	4.3	16^{+9}_{-2}	$9.4^{+0.6}_{-9.3}$	O9+V [C16]

Table A2. List of detected sources in the centre of R136 brighter than 16 mag in K. ID_K is the star's identification in our K catalogue. K(2018) and H(2018) are the K and H magnitudes of stars in the second epoch data in 2018. K(2015) and J(2015) are the K and J magnitudes of stars in the first epoch data in 2015. HSH95 and WB85 are the stars' identification in Hunter et al. (1995) and Weigelt & Baier (1985), followed by their U, V, and I magnitudes in the *HST*/WFPC2 filters. Last column is V–K (F555W-K(2018)). See Fig. A2 for their positions in the image.

ID_K	K (2018)	H (2018)	K (2015)	J (2015)	HSH95 (WB85)	U (F336W)	V (F555W)	I (F814W)	(V–K)
1	11.15	11.29	11.07	11.33	3 (a1)	11.56	12.84	12.18	1.69
2	11.31	11.98	11.48	11.78	10 (c)	12.52	13.47	12.71	2.16
3	11.43	11.70	11.32	11.55	5 (a2)	11.94	12.96	12.48	1.53
4	11.45	11.73	11.44	11.77	6 (a3)	11.86	13.01	12.46	1.56
5	11.67	11.90	11.66	11.67	9 (b)	12.29	13.32	12.76	1.65
6	12.79	12.76	12.73	12.75	20 (a5)	12.77	13.93	13.54	1.14
7	13.04	13.18	13.05	13.24	26	12.89	14.19	13.64	1.15
8	13.05	13.05	12.96	12.86	36	13.36	14.49	13.98	1.44
9	13.14	13.06	13.09	13.00	21 (a4)	12.81	13.96	13.63	0.82
10	13.17	13.73	13.36	13.52	57	14.03	14.87	14.23	1.70
11	13.18	13.30	13.19	13.28	19 (a6)	12.86	13.92	13.72	0.74
12	13.33	13.50	13.45	13.37	17	13.00	13.78	13.89	0.45
13	13.35	13.20	13.05	12.95	24 (a7)	12.84	14.06	13.66	0.71
14	13.41	13.27	13.27	13.18	27 (a8)	12.93	14.22	13.86	0.81
15	13.42	13.32	13.29	13.11	46	13.64	14.73	14.26	1.31
16	13.49	13.82	13.58	13.37	59	13.81	14.88	14.35	1.39
17	13.51	13.36	13.32	13.17	47	13.64	14.75	14.31	1.24
18	13.60	13.80	13.62	13.69	31	13.14	14.41	14.08	0.81
19	13.68	13.62	13.58	13.41	48	13.61	14.78	14.37	1.10
20	13.69	13.74	13.63	13.37	45	13.51	14.68	14.31	0.99
21	13.73	13.69	13.65	13.62	30	13.09	14.32	14.02	0.59
22	13.83	14.41	13.84	14.33	124	999.99	15.97	15.46	2.14
23	13.86	13.72	13.72	13.61	40	13.32	14.60	14.35	0.74
24	13.87	13.77	13.78	13.70	39	13.31	14.59	14.31	0.72
25	13.92	14.08	13.99	14.23	33	13.07	14.43	14.19	0.51
26	13.93	14.04	13.84	13.73	102	14.75	15.70	15.10	1.77
27	13.94	13.97	13.85	13.67	65	14.03	15.18	14.49	1.24
28	13.97	13.98	13.96	13.82	50	13.62	14.81	14.48	0.84
29	14.01	13.86	13.84	13.69	64	14.01	15.12	14.68	1.11
30	14.01	14.10	13.93	14.07	111	14.94	15.77	15.20	1.76
31	14.01	14.11	13.96	13.63	68	14.13	15.22	14.76	1.21
32	14.01	15.05	14.68	14.94	38	13.28	14.57	14.11	0.56
33	14.02	13.91	13.91	13.78	58	13.65	14.88	14.55	0.86
34	14.04	14.03	14.00	14.04	35	13.35	14.48	14.27	0.44
35	14.05	14.18	14.11	14.30	42	13.35	14.63	14.58	0.58
36	14.06	14.28	14.15	14.15	55	13.62	14.86	14.53	0.80
37	14.08	13.96	13.98	13.94	49	13.55	14.80	14.53	0.72
38	14.16	15.05	14.64	15.30	29	12.89	14.30	14.03	0.14

Downloaded from https://academic.oup.com/mnras/article/503/1/292/6133467 by CNRS - ISTO user on 07 June 2022

Table A2 – *continued*

ID_K	K (2018)	H (2018)	K (2015)	J (2015)	HSH95 (WB85)	U (F336W)	V (F555W)	I (F814W)	(V–K)
39	14.17	14.28	14.20	14.10	52	13.52	14.82	14.55	0.65
40	14.31	14.16	14.20	14.06	70	13.93	15.23	14.80	0.92
41	14.36	14.41	14.35	14.28	62	13.72	15.02	14.75	0.66
42	14.45	14.49	14.39	14.29	69	14.02	15.22	15.03	0.77
43	14.45	14.44	14.42	14.31	66	13.95	15.19	14.88	0.74
44	14.46	14.44	14.38	14.24	73	14.16	15.27	15.01	0.81
45	14.50	15.48	14.84	15.29	262	16.08	16.92	16.18	2.42
46	14.58	14.88	14.70	14.80	71	14.01	15.23	15.00	0.65
47	14.63	14.82	14.80	14.80	86	14.23	15.49	15.19	0.86
48	14.65	15.10	14.79	14.80	136	15.14	16.06	15.58	1.41
49	14.67	14.76	14.68	14.76	78	14.11	15.34	15.05	0.67
51	14.72	14.68	14.49	14.77	107	14.58	15.74	15.34	1.02
52	14.72	14.69	14.72	14.56	77	13.97	15.30	14.99	0.58
53	14.76	14.70	14.64	14.42	118	14.79	15.89	15.45	1.13
54	14.77	14.83	14.77	14.71	80	14.13	15.35	15.12	0.58
55	14.79	14.82	14.78	14.84	75	13.89	15.28	15.06	0.49
56	14.81	14.70	14.61	14.49	177	15.35	16.31	15.76	1.50
57	14.81	14.80	14.69	14.62	89	14.39	15.52	15.21	0.71
58	14.83	15.18	14.97	14.92	87	14.32	15.50	15.28	0.67
59	14.83	14.86	14.83	14.88	90	14.30	15.55	15.29	0.72
60	14.84	14.92	14.85	14.69	94	14.32	15.60	15.30	0.76
61	14.84	14.79	14.70	14.43	129	14.97	16.03	15.65	1.19
62	14.86	14.82	14.78	14.81	93	14.34	15.60	15.24	0.74
63	14.87	15.22	15.02	14.96	97	14.43	15.61	15.36	0.74
64	14.90	14.94	14.87	14.96	92	14.28	15.59	15.38	0.69
65	14.91	15.15	15.03	15.34	79	13.98	15.35	15.09	0.44
66	14.96	15.41	15.10	15.39	219	15.81	16.68	16.03	1.72
67	14.96	14.80	14.78	14.61	112	14.63	15.77	15.45	0.81
68	14.97	15.84	15.75	17.21	623	18.01	18.41	17.45	3.44
69	15.10	15.09	14.98	14.93	193	15.66	16.51	16.03	1.41
70	15.12	15.61	15.32	15.22	183	15.33	16.35	15.85	1.23
71	15.14	15.83	15.50	16.08	84	14.20	15.48	15.20	0.34
72	15.21	15.38	15.26	15.33	114	14.51	15.82	15.59	0.61
73	15.21	15.28	15.16	14.93	222	15.76	16.70	16.21	1.49
74	15.23	15.25	15.18	15.17	119	15.00	15.92	15.88	0.69
75	15.24	15.14	15.11	14.93	143	14.89	16.10	15.76	0.86
77	15.28	15.33	15.27	15.42	127	14.80	16.02	15.73	0.74
78	15.29	15.42	15.22	15.33	149	14.94	16.14	15.85	0.85
79	15.30	15.38	15.22	15.03	277	16.07	16.97	16.41	1.67
80	15.31	15.31	15.25	15.24	150	14.97	16.16	15.85	0.85
81	15.31	15.63	15.47	15.50	121	14.81	15.96	15.70	0.65
82	15.32	15.60	15.45	15.86	116	14.64	15.85	15.60	0.53
83	15.35	16.50	15.98	16.73	76	13.92	15.29	15.11	−0.06
84	15.38	15.96	15.63	15.60	197	15.49	16.53	16.04	1.15
85	15.38	15.62	15.23	15.70	213	15.70	16.65	16.38	1.27
86	15.40	15.41	15.33	15.35	165	15.14	16.23	15.91	0.83
87	15.40	15.46	15.40	15.33	141	14.74	16.09	15.80	0.69
88	15.40	16.49	15.96	15.97	125	14.84	15.98	15.72	0.58
89	15.43	15.38	15.33	15.08	207	15.72	16.62	16.28	1.19
90	15.44	15.28	15.32	15.17	135	14.89	16.05	15.79	0.61
91	15.45	15.35	15.36	15.38	132	14.77	16.04	15.81	0.59
92	15.47	15.62	15.51	15.51	159	15.07	16.21	15.90	0.74
93	15.48	16.05	15.75	16.11	120	14.76	15.95	15.69	0.47
94	15.48	16.10	15.78	15.85	128	14.91	16.02	15.76	0.54
95	15.49	15.83	15.61	15.88	123	14.76	15.96	15.70	0.47
96	15.49	15.58	15.47	15.31	205	15.49	16.59	16.23	1.10
97	15.50	15.58	15.42	15.21	189	15.35	16.46	16.13	0.96
98	15.51	16.36	15.98	15.97	153	14.99	16.17	15.86	0.66
99	15.54	15.91	15.71	15.90	134	14.83	16.05	15.82	0.51
100	15.54	15.75	15.46	15.77	480	17.40	17.91	17.01	2.37
101	15.54	15.79	15.66	15.98	162	15.04	16.23	15.92	0.69
102	15.55	15.57	15.59	15.71	108	14.65	15.74	15.49	0.19

Downloaded from https://academic.oup.com/mnras/article/503/1/292/6133467 by CNRS - ISTO user on 07 June 2022

Table A2 – *continued*

ID_K	K (2018)	H (2018)	K (2015)	J (2015)	HSH95 (WB85)	U (F336W)	V (F555W)	I (F814W)	(V–K)
103	15.55	15.71	15.53	15.23	224	15.56	16.71	16.30	1.16
104	15.55	15.54	15.51	15.56	170	15.09	16.27	15.97	0.72
105	15.56	15.78	15.64	15.72	139	14.80	16.08	15.86	0.52
106	15.56	15.65	15.58	15.76	137	14.78	16.06	15.80	0.50
107	15.57	16.16	15.79	15.75	230	15.75	16.76	16.35	1.19
108	15.58	15.42	15.43	15.24	184	15.30	16.42	16.11	0.84
109	15.58	15.88	15.54	15.95	652	18.00	18.50	18.05	2.92
111	15.62	15.45	15.46	15.53	115	14.70	15.83	15.65	0.21
112	15.63	15.86	15.67	15.55	255	15.94	16.91	16.47	1.28
113	15.64	16.02	15.83	16.28	145	14.93	16.12	15.88	0.48
115	15.65	15.56	15.45	15.23	250	16.03	16.89	16.49	1.24
116	15.68	16.37	16.04	16.60	140	14.90	16.08	15.81	0.40
117	15.68	15.96	15.67	15.61	272	16.17	16.96	16.49	1.28
118	15.69	15.51	15.52	15.38	179	15.13	16.32	16.10	0.63
119	15.70	15.76	15.56	15.52	449	17.18	17.81	17.15	2.11
120	15.70	16.28	16.04	16.40	117	14.60	15.86	15.71	0.16
121	15.71	15.63	15.63	15.70	173	15.00	16.28	16.10	0.57
122	15.75	16.03	15.88	16.10	181	15.20	16.34	16.05	0.59
123	15.77	16.05	15.85	15.83	258	15.86	16.92	16.42	1.15
125	15.79	15.67	15.64	15.35	271	15.94	16.96	16.55	1.17
126	15.81	15.77	15.80	15.79	176	15.02	16.30	16.07	0.49
127	15.82	16.19	15.74	16.44	488	17.17	17.93	17.26	2.11
128	15.82	15.70	15.69	15.58	231	15.68	16.77	16.42	0.95
129	15.83	15.68	15.68	15.55	206	15.43	16.60	16.34	0.77
130	15.86	15.95	15.90	15.83	187	15.12	16.44	16.20	0.58
132	15.88	16.25	15.98	15.92	236	15.72	16.82	16.47	0.94
133	15.91	16.05	15.95	16.06	217	15.47	16.67	16.39	0.76
134	15.91	16.36	15.76	16.52	814	19.33	19.01	18.21	3.10
135	15.93	15.98	15.87	15.90	290	16.11	17.04	16.61	1.11
136	15.95	15.89	15.88	15.81	210	15.41	16.64	16.42	0.69
137	15.95	16.35	16.08	16.37	225	15.66	16.72	16.38	0.77
138	15.95	16.94	16.45	17.21	151	15.04	16.16	15.91	0.21
139	15.95	16.23	16.03	15.86	294	16.00	17.06	16.68	1.11
140	15.95	17.08	16.49	16.53	209	15.70	16.64	16.27	0.69
141	15.97	16.17	16.02	16.17	233	15.71	16.78	16.52	0.81
142	15.97	16.06	15.87	15.90	415	16.81	17.64	17.08	1.67
143	15.97	17.20	16.57	16.90	147	14.92	16.13	15.91	0.16
144	16.00	15.78	15.81	15.58	285	15.93	17.01	16.67	1.01

Table A3. Sample catalogue of detected sources in H and K data in 2018. Full table is available online. ID_K is the star's identification in our *K*-band catalogue. K and H are the K and H magnitudes of stars in 2018. $Correlation_H$ and $Correlation_K$ are the correlation between the PSF of detected source with the reference PSF in H and K images. σ is the photometric error estimated for the positions and magnitudes.

ID_K	X (pix)	σ_x (pix)	Y (pix)	σ_y (pix)	K	σ_K	$Correlation_K$	H	σ_H	$Correlation_H$
1	476.82	0.00	517.37	0.00	11.15	0.00	0.96	11.29	0.00	0.97
2	256.56	0.00	354.97	0.00	11.31	0.00	0.97	11.98	0.00	0.97
3	468.62	0.00	521.19	0.00	11.43	0.00	0.98	11.70	0.00	0.94
4	503.11	0.00	489.78	0.00	11.45	0.00	0.99	11.73	0.00	0.95
5	325.86	0.00	442.90	0.00	11.67	0.00	1.00	11.90	0.00	0.95
6	459.19	0.00	532.97	0.00	12.79	0.00	1.00	12.76	0.00	0.93
7	520.87	0.00	479.45	0.00	13.04	0.00	0.80	13.18	0.00	0.90
8	355.58	0.00	520.89	0.00	13.05	0.00	0.97	13.05	0.00	0.98
9	497.73	0.00	543.72	0.00	13.14	0.00	0.95	13.06	0.00	0.99
10	231.27	0.00	332.67	0.00	13.17	0.00	0.98	13.73	0.00	0.98

This paper has been typeset from a TEX/LATEX file prepared by the author.

Downloaded from https://academic.oup.com/mnras/article/503/1/292/6133467 by CNRS - ISTO user on 07 June 2022